nature communications

Article

https://doi.org/10.1038/s41467-026-71768-3

Reticulate leaf venation in *Pilea peperomioides* is a Voronoi diagram

Received: 1 July 2024

Accepted: 30 March 2026

Published online: 12 May 2026

Check for updates

CiCi Xingyu Zheng[1], Shirsa Palit[1], Matthew Venezia[1], Elijah Blum[1], Ullas V. Pedmale[1], Dave Jackson[1], Enrico Scarpella[2], Przemyslaw Prusinkiewicz[3] ✉ & Saket Navlakha[1] ✉

Reticulate leaf venation, characterized by the presence of loops, is a distinguishing feature of many flowering plants. However, our understanding of both the geometry and the morphogenesis of reticulate vein patterns is far from complete. We show that in the Chinese money plant (*Pilea peperomioides*), major veins form an approximate Voronoi diagram surrounding secretory pores known as hydathodes. We also propose a mechanistic model based on polar transport of the plant hormone auxin to produce Voronoi patterns, and we support this model with experimental evidence. In contrast to classical models where veins directly connect auxin sources to sinks, our model generates veins that bisect the space between adjacent auxin sources, collectively forming loops. The paradigm change offered by this model may open the door to study reticulate vein formation in other species.

The quest to characterize natural forms in precise, mathematical terms has a history spanning centuries[1]. In general, these characterizations belong to three categories. *Partial descriptions* characterize some aspects of form, but are not comprehensive enough to reconstruct them; examples include symmetry, allometric scaling (e.g., brain size scaling across mammals)[2,3] and self-similarity (e.g., broccoli)[4]. *Total descriptions*, by contrast, characterize an entire form; examples include the spiral shapes of sea shells[5] and phyllotaxis (e.g., seed arrangement in the sunflower head)[6]. *Generative models* explain how observed forms develop using local interactions; examples include reaction-diffusion models of pattern formation (e.g., digit formation)[7] and Lindenmayer system models of branching structures (e.g., plant shoot architecture)[8]. The ultimate goal is to obtain a comprehensive characterization of form consistent with the partial descriptions, and a mechanistic model of its emergence. Here, we seek a comprehensive description and corresponding generative model for reticulated leaf veins.

Despite both their ubiquity in nature and accessibility to study, reticulate (i.e., closed loop) venation patterns have only been partially characterized, with few plausible generative models. Partial descriptions include the geometric relationships between branch radii and branch angles[9,10]; the spatial distribution of veins across a leaf blade[11–13]; the hierarchical nesting and ordering of loops[14–16], including their sizes and shapes[17]; and how loops provide robustness to vein damage and flow fluctuations[18,19]. Generative models of venation patterning at the molecular level are dominated by Sachs' canalization hypothesis[20–22], which attributes the patterning of veins to positive feedback between the plant hormone auxin and its transporters. These models, however, typically produce tree-like branching patterns, as opposed to closed loops[23–27]. Together, these descriptions and models remain inadequate to explain the development of reticulated veins using plausible molecular mechanisms.

Voronoi diagrams[28–30] are geometric patterns that have been studied for centuries in both computational geometry and mathematical biology. A Voronoi diagram is a partitioning of space into polygons (i.e., closed loops), each surrounding a given generator point, which we refer to as a polygon "center". This diagram has the property that all the points within a polygon are closer to that polygon's center than any other center. For example, when partitioning a town (space) into school districts (polygons), a Voronoi diagram guarantees that all students living within a district are closer to that district's school (center) than any other school, thus minimizing distances traveled. Although Voronoi diagrams are often used as an analytical tool to interpret biological patterns, such as cell packing, tissue segmentation, or growth forms of plants competing for light, water or nutrients[28,31–33],

[1]Cold Spring Harbor Laboratory, Cold Spring Harbor, NY, USA. [2]University of Alberta, Edmonton, AB, Canada. [3]University of Calgary, Calgary, AB, Canada. ✉e-mail: pwp@ucalgary.ca; navlakha@cshl.edu

there are not many examples of Voronoi diagrams emerging naturally in biological structures. Moreover, while some structures found in nature seem to resemble Voronoi diagrams[34], in most of these examples (e.g., giraffe skin patterns[35] or secondary veins of dragonflies[36]) only the polygon boundaries but not the centers are present (Supplementary Note 1). Thus, rigorously testing whether these examples are naturally occurring Voronoi diagrams is not straightforward.

We discovered that in *Pilea peperomioides*, commonly known as the Chinese money plant, Voronoi diagrams are an approximate global descriptor of vein reticulation. To our knowledge, this is the first demonstration of the occurrence of Voronoi diagrams in plant venation patterns, where both edges and centers are visible and functional. We also propose a generative model that approximates these patterns using a biologically plausible mechanism and present supporting experimental evidence. This model represents an alternative to the canalization hypothesis and offers a new direction for investigating the morphogenesis of reticulated networks in plants.

Results

Pilea as a model system for reticulate vein patterns

Pilea peperomioides (Fig. 1a) is an angiosperm from the *Urticaceae* family, native to southern China[37]. The plant has peltate orbicular leaves, characterized by an almost round leaf blade supported by a petiole attached to the leaf underside (Fig. 1b).

We studied the relationship between two structures found on Pilea leaves: hydathodes and veins (Fig. 1c). Hydathodes are secretory pores and guttation sites found on the leaves of many plant species. These pores perform numerous functions, including releasing excess water to regulate hydraulic balance[38], removing harmful chemicals[38], and regulating immune responses against leaf-invading microbes[39]. Compared to stomata, hydathodes are roughly an order of magnitude larger, allow for uni-directional flow (as opposed to bi-directional gas exchange), and are static structures that remain open.

The vein network of a mature Pilea leaf is composed of two types of primary veins, four types of secondary veins, and a mesh of higher-order, minor veins (Fig. 1c). Both types of primary veins run the length of the leaf: the midvein vein runs at the leaf center, and the two lateral veins run at the side of the midvein. The three primary veins join at the point of leaf attachment to the petiole and again at the tip of the leaf. Each of the four types of secondary veins run in a different area of the leaf: interior veins run between the midvein and the lateral veins; the peri-marginal vein runs along the leaf margin; exterior veins run between lateral veins and the peri-marginal vein; and trans-marginal veins connect exterior veins with the peri-marginal vein. The major veins, encompassing both primary and secondary veins, form polygon-shaped closed loops surrounding the hydathodes[40]. Finally, minor veins form a mesh of veinlets that connect hydathodes to lower-order veins, completing the vascular system. In this study, we primarily characterize and study the development of secondary veins (i.e., those that surround hydathodes).

We imaged flattened Pilea leaves using light microscopy and developed a semi-automated computational pipeline to extract the two-dimensional positions of all hydathodes, as well as the network structure formed by major veins (Fig. 1d, and Supplementary Fig. 1; Methods). We analyzed 34 leaves from 6 Pilea plants, grown in indoor conditions (Methods). Most minimal polygons (i.e., polygons that contain no other polygons) formed by major veins contained exactly one hydathode (73.11%), and the remaining polygons contained either zero (10.26%) or >1 hydathodes (16.63%), which we discuss later. Polygons in each leaf had a wide spread of sizes and aspect ratios (Supplementary Table 1).

A geometric framework to quantify Voronoi patterning

Given a set of n centers in two-dimensional space, a Voronoi diagram consists of a set of n polygons $\mathcal{P} = \{P_1, P_2, \ldots, P_n\}$, each enclosing a single center, such that all points p within polygon P_i are closer to center i than any other center $j \neq i$:

$$P_i = \{p : d(p,i) < d(p,j) \quad \forall j \neq i\}, \tag{1}$$

where $d(\cdot,\cdot)$ denotes Euclidean distance. The boundaries of polygons are formed along points that are equidistant to adjacent centers.

Due to stochasticity and developmental constraints, it is unlikely that a naturally formed venation patterning will perfectly satisfy the Voronoi property in Equation (1) (Fig. 1e). Thus, we developed three tests to quantify how close a given patterning is to matching the Voronoi property. These tests, described next, measure: **I)** how well local geometric relationships between hydathodes and veins follow those of an ideal Voronoi diagram; **II)** how well vein locations can be predicted given only hydathode locations as input; and **III)** how well hydathode locations can be predicted given only vein locations as input. We also applied these tests to tessellations that would be generated if each center (i.e., the hydathode) were located at three alternative reference locations within a

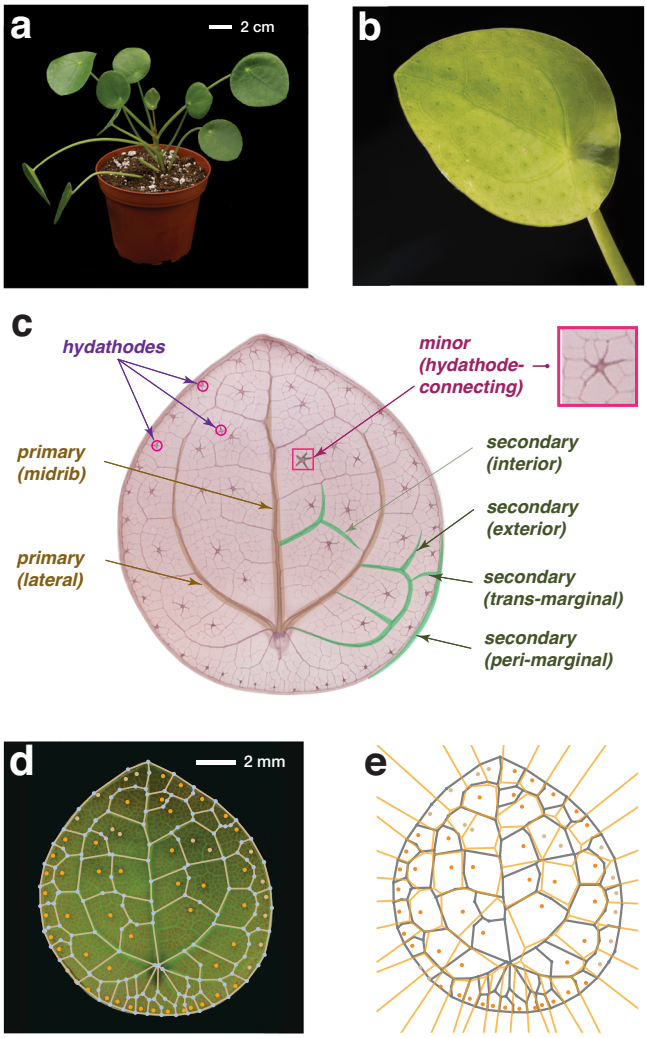

Fig. 1 | Major veins and hydathodes in *Pilea peperomioides* form a Voronoi-like diagram. a The Pilea plant. **b** Close-up view of a young leaf. **c** A sample cleared leaf, with vasculature and hydathodes stained with safranin, and leaf anatomy labeled. **d** The same leaf under light microscopy, with the network of the major veins (white edges) and hydathodes (orange dots) traced. Representative example of 34 leaves imaged. **e** Overlay of actual major veins (blue lines) with an exact Voronoi diagram (orange lines) constructed using hydathodes as the polygon centers.

https://doi.org/10.1038/s41467-026-71768-3

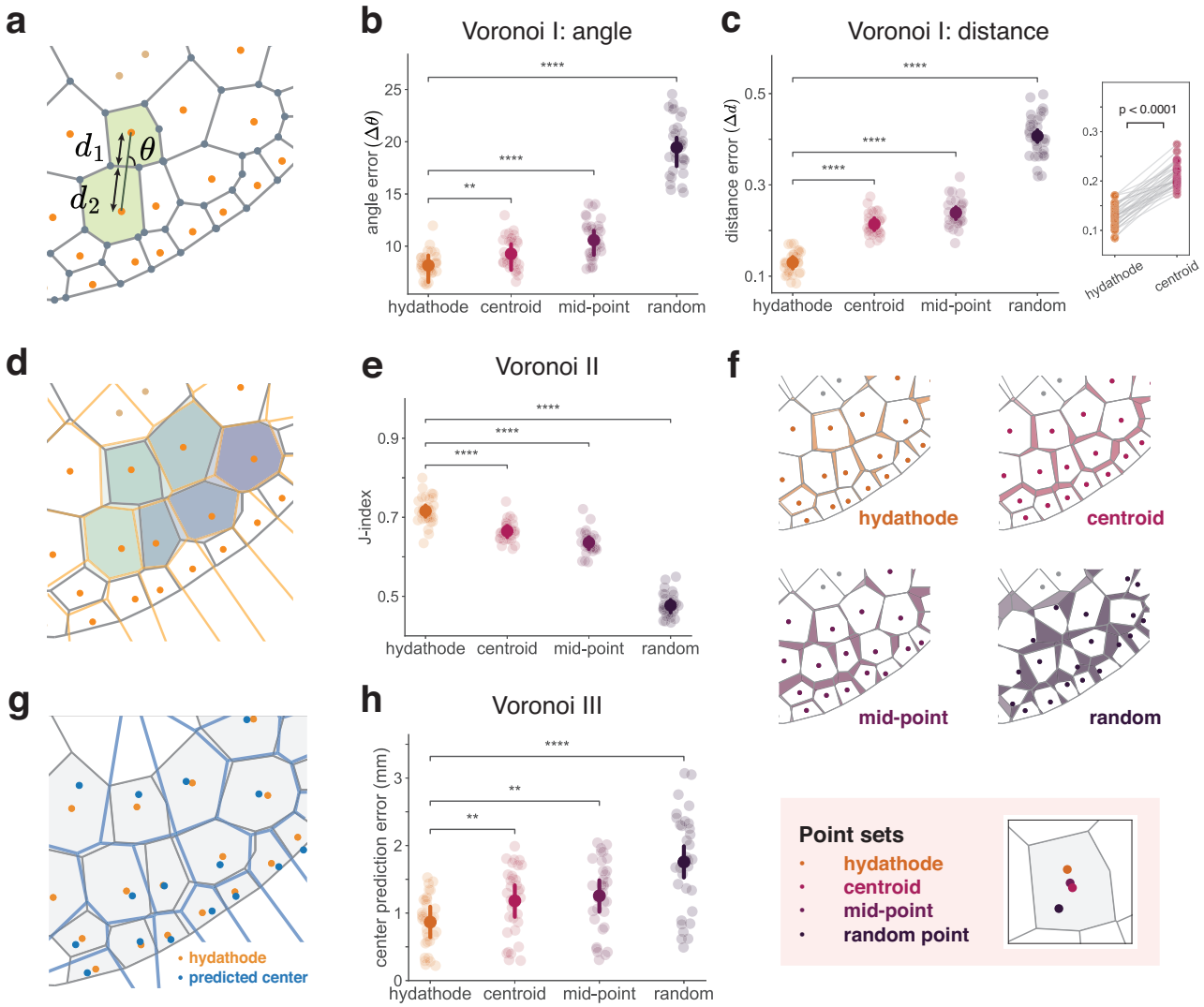

Fig. 2 | The Voronoi diagram approximation in Pilea is supported by three statistical tests. a Schematic for the Voronoi I test, applied to each neighboring polygon pair. **b** Voronoi I test result ($n = 34$) for the angle error ($\Delta\theta$). In panels (**b**), (**c**), (**e**), and (**h**), the mean and 95% confidence interval of the estimated posterior mean are plotted in the foreground. **c** Voronoi I test result ($n = 34$) for distance error (Δd). Inset highlights pairwise comparison between errors computed with hydathodes vs. centroids. **d** Schematic for Voronoi II test. Overlay of the Pilea major veins (gray) and Voronoi diagram edges (orange) using hydathodes as the centers. Unions and intersections of corresponding polygons in the two tessellations are shaded and used to calculate the Jaccard Index. **e** Voronoi II test results ($n = 34$). **f** Visualization of the pattern mismatch between polygons formed by secondary veins in Pilea and the Voronoi diagrams generated by hydathodes vs. other reference point sets. **g** Schematic for Voronoi III test. Overlay of the Pilea major veins (gray), hydathodes (orange) with the predicted center location (blue dots), and the Voronoi diagram (blue edges) generated using the predicted centers. **h** Voronoi III test results ($n = 33$). Statistical comparisons wered performed using one-sided Bayesian generalized linear mixed-effects models with Bonferroni correction applied across three pairwise comparisons. Asterisks indicate significance based on the probability of direction: * $p < 0.05$, ** $p < 0.01$, *** $p < 0.001$.

polygon: 1) the centroid of the polygon (i.e., its gravitational center), which is often used as a proxy for center locations when centers are absent[41,42]; 2) the mid-point of the polygon: produced by sliding a horizontal line through the polygon in the vertical direction along the mid-vein, stopping when the line is mid-way through the polygon, and finding the mid-point of the line segment bounded by the polygon edges; and 3) random points picked within the polygon.

Pilea hydathodes and major veins form a near-exact Voronoi diagram

Voronoi test I: angle and distance conditions. A corollary of the Voronoi property (Equation (1)) is that the line segment connecting the centers of adjacent polygons should perpendicularly bisect the shared edge of the two polygons (Fig. 2a). This means that the angle (θ) formed by the line segment and the shared boundary should be 90 degrees, and that the two distances (d_1, d_2) from each adjacent center to the shared boundary should be equal. We defined the angle error to be $\Delta\theta = |90 - \theta|$, and the (normalized) distance error to be $\Delta d = |d_1 - d_2|/(d_1 + d_2)$. Smaller errors indicate a closer match to an ideal Voronoi diagram. We computed the angle and distance errors for all 1836 adjacent pairs of major vein polygons (that each contained a single hydathode) across all 34 leaves (Supplementary Table 1).

The errors induced when using the hydathode locations as Voronoi centers were less than when using the three other reference locations (Fig. 2b, c). Specifically, the angle error for hydathodes was 8.23 ± 1.13 degrees (mean ± standard deviation), significantly smaller than 9.35 ± 1.47 for centroids, 10.65 ± 1.82 for mid-points, and 19.51 ± 2.48 for random points (Fig. 2b) (Methods; Supplementary Table 2). Similarly, the distance error for hydathodes was 0.13 ± 0.02 mm, which was significantly less than that of the other

reference locations: 0.21 ± 0.02 for centroids, 0.24 ± 0.03 for mid-points, and 0.41 ± 0.04 for random points (Fig. 2c; Supplementary Table 2). Thus, the spatial arrangement of hydathodes and major vein polygons closely followed the local geometry of a Voronoi diagram.

Voronoi Test II: Predicting veins given hydathode locations. If a true Voronoi diagram were constructed given actual hydathode locations as input, how much overlap would there be between the true Voronoi polygons and the actual polygons formed by major veins? To quantify this, we measured the average area overlap between the true Voronoi polygons and corresponding observed (major vein) polygons (Fig. 2d):

$$J = \frac{1}{N}\sum_{i}\frac{|A^{(i)}_{\text{true}} \cap A^{(i)}_{\text{obs}}|}{|A^{(i)}_{\text{true}} \cup A^{(i)}_{\text{obs}}|}, \quad (2)$$

where N is the number of single-hydathode polygons on the leaf, and $A^{(i)}_{\text{true}}$ and $A^{(i)}_{\text{obs}}$ are sets of points in the polygon for center i in the true Voronoi diagram and the corresponding major vein polygon, respectively. This measure, called the Jaccard index, ranges from 0 to 1, with larger values indicating more overlap.

The overlap between true and observed polygons formed by secondary veins was higher when using hydathodes as centers, compared to when using the other reference locations (Fig. 2e). Specifically, the overlap for hydathodes was 0.72 ± 0.03, which is significantly higher compared to 0.67 ± 0.02, 0.64 ± 0.03, and 0.47 ± 0.03 for centroid, mid-point, and random centers, respectively (Supplementary Table 2). These differences are visually pronounced (Fig. 2f), especially at the periphery of the leaf blade, where the true and hydathode-predicted boundaries are particularly well-aligned. The largest mismatch between the true and hydathode-predicted boundaries occurred around the primary veins (Supplementary Fig. 6), which suggests that primary veins may be patterned by a mechanism different from that which patterns secondary veins.

To measure how much biological noise would be required to match the observed deviation from a Voronoi diagram, we added random noise at each true Voronoi vertex (i.e., at locations where two polygon boundaries intersect) and calculated the Jaccard index between the true (noise-free) Voronoi polygons and those formed after noise was added. The overlap between the noise-free and noisy Voronoi diagrams matched the observed overlap (0.72) when about 15% noise was added (Supplementary Fig. 2a, b). Thus, the observed deviations were commensurate with the ideal Voronoi with a small amount of noise.

To test if an alternative spatial tessellation model can generate polygons similar to Pilea major vein polygons, we applied a variant of the *k-d* tree (Methods), which recursively generates rectangles surrounding hydathodes until all pairs of adjacent hydathodes are bisected by a rectangle edge (Supplementary Fig. 2c–e). This model uses a hierarchical spatial sub-division principle shared with the venation process[43–45], and it generates perpendicular bisections between adjacent cell edges and centers. However, the overlap between the *k-d* tree tessellation and the major vein polygons was 0.40 ± 0.03, which was on par with the overlap for random points (0.47). Thus, Voronoi diagrams are a more likely candidate model than a *k-d* tree to describe the relationship between hydathodes and major veins.

Voronoi Test III: Predicting hydathode locations given veins. Given the polygons formed by major veins, how well can we predict the locations of the enclosed hydathodes? This is called the "inverse Voronoi" problem[46], and our goal here was to solve for the center locations that minimize the angle and distance errors for a given tessellation (Methods)[47].

We found that the optimal Voronoi center locations were significantly closer to the actual hydathode locations than any of the three reference locations (Fig. 2g, h). Specifically, hydathode locations were 0.87 ± 0.38 mm from the true Voronoi center locations, compared to 1.18 ± 0.50 mm for centroid, 1.25 ± 0.53 mm for mid-point, and 1.76 ± 0.72 mm for random points (Supplementary Table 2). This suggests that hydathodes are located near the true Voronoi centers of major vein polygons.

In general, these three Voronoi tests can be applied to determine how close any natural Voronoi-like diagram is to a true Voronoi diagram. To verify their stringency, we applied them to another biological spatial tessellation: the air chambers (polygons) surrounding air pores (centers) on leaf-like structures (thalluses) in the liverwort *Marchantia polymorpha* (Supplementary Fig. 3, and Supplementary Note 5). We found that air pore locations deviated more from a true Voronoi diagram compared to centroid locations, and the Voronoi test errors for the liverwort thallus were larger than those in Pilea (Supplementary Tables 2, 3). This suggests that Marchantia air chambers and pores do not form a Voronoi diagram, and that our tests indeed have the statistical power to distinguish Voronoi-like patterns from other non-Voronoi spatial tessellations.

The Pilea Voronoi property is robust across stress conditions. To test whether stress induces deviations from the Voronoi geometry, we exposed Pilea plants to light or heat stress (Fig. 3a), conditions which impact hydathode morphology[38,48] and vein patterning[49], respectively. We grew 6 plants in each of three stress conditions, namely shade, high-light intensity, and high-temperature, and collected 128 new leaves that emerged during a five-week treatment period (Methods). Pilea exhibited various phenotypic changes in response to these conditions, especially changes in leaf morphology (Supplementary Fig. 4a–e; and Supplementary Note 2). For example, hydathode sizes varied significantly across conditions (Fig. 3b): in high-temperature, hydathodes were significantly larger than in controls, suggesting that hydathode size is regulated to manage water loss. These conditions also led to variation in leaf color and size, though not in the number of hydathodes (Supplementary Table 1; Supplementary Note 2). Specifically, the histogram of hydathode counts in each condition followed a right-skewed unimodal distribution with means that were not significantly different (Supplementary Fig. 4f–g). While there was stochasticity in exact hydathode locations across leaves in different conditions, the underlying spatial distribution of hydathodes was similar (Fig. 3c; and Supplementary Note 3). Moreover, the number of hydathodes per leaf could be described by a simple Poisson distribution centered at the average of all samples combined (Fig. 3d).

Despite these changes in leaf morphology, hydathodes and major vein polygons still formed near-exact Voronoi diagrams (Supplementary Fig. 5) according to the three Voronoi tests. Moreover, the level of deviation from being a true Voronoi diagram was low for the stressed plants, similar to the controls (Supplementary Table 2, S3). This indicates that these stress conditions (a) do not disturb the Voronoi geometry between veins and hydathodes, and (b) do not alter the relatively uniform character of leaf expansion (growth), reflected in the round shape of Pilea leaves irrespective of their size (Supplementary Fig. 15), which would otherwise distort an initial Voronoi pattern. In addition, the preservation of Voronoi-like patterning in the presence of stress-induced variation in the number and location of hydathodes implies that this pattern is not pre-specified in development, and that a local, self-regulatory mechanism might be at play.

Voronoi-like vasculature patterns in Pilea leaves can be patterned by auxin

A key question is the molecular mechanism giving rise to the observed relation between hydathodes and vascular patterning in Pilea. The prevalent theory for vein formation is canalization, proposed by Sachs more than half a century ago, which attributes the

https://doi.org/10.1038/s41467-026-71768-3

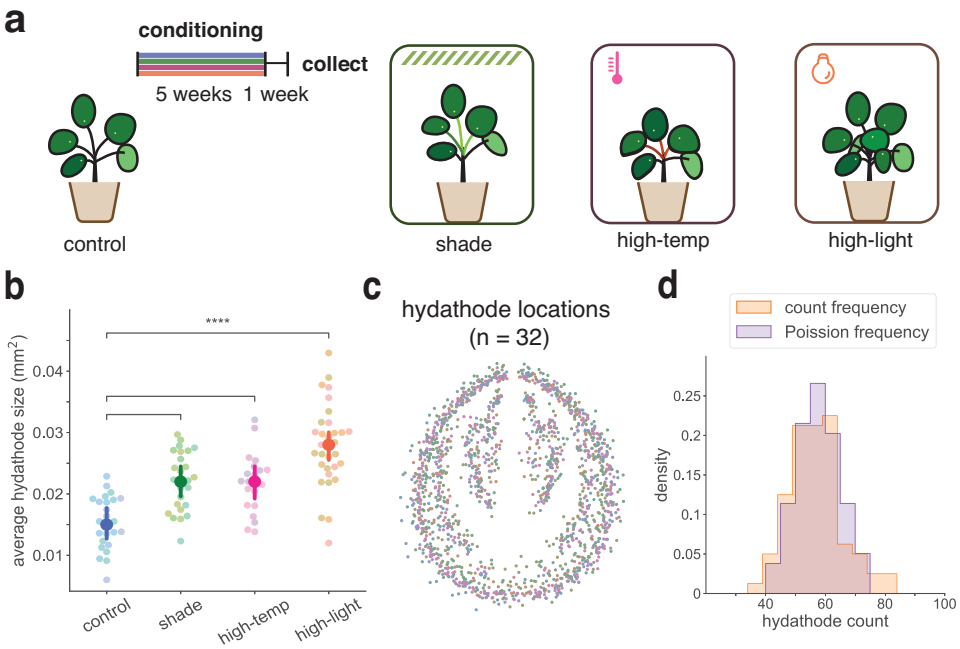

Fig. 3 | The Pilea Voronoi property is preserved under environmental stress. **a** Schematic of environmental conditioning experiments. Pilea plants were exposed to four conditions: control (indoors with indirect natural light), shade, high temperature, and high light intensity. **b** Mean hydathode size in control and treatment conditions ($n = 20$ each). The mean and 95% confidence interval of the estimated posterior mean are plotted in the foreground, and the colors of the scatter plot in the background are coded by plants. Statistical comparisons were performed using one-sided Bayesian generalized linear mixed-effects models with Bonferroni correction applied across three pairwise comparisons. Asterisks indicate significance based on the probability of direction: * $p < 0.05$, ** $p < 0.01$, *** $p < 0.001$. **c** Overlay of hydathode locations ($n = 32$ samples over all treatment conditions). **d** Relative frequencies of the hydathode count distribution ($n = 80$) and of the Poisson distribution with the same mean.

patterning of vascular strands to a positive feedback between auxin flow and the polarization of auxin transporters[20–22]. Predating molecular evidence, Mitchison[23,50,51] used a computational model to demonstrate that, if this feedback is strong enough, auxin flowing from auxin sources to sinks will become channeled into gradually narrowing paths with high auxin flux (canals), the precursors of veins. The subsequent discovery of auxin efflux carriers (PINs), and the visualization of PIN and auxin response reporter proteins, lent further credence to the hypothesis that auxin and its transporters are central to vein patterning[52–55]. Follow-up computational models further confirmed that strong feedback between auxin flux and PINs can reproduce midvein formation[24] and open branching patterns[25]. However, the Voronoi-like relation between hydathodes and major veins in Pilea leaves is at odds with canalization. In Arabidopsis, hydathodes are sites of high auxin concentration[56–58], which suggests that, in general, they act as auxin sources; and yet in Pilea, major veins run between the hydathodes, separating rather than connecting them. This raises the question of whether an alternative mode of interaction between auxin and PINs could explain the patterning of major veins in Pilea.

We addressed this question using computational models. We hypothesized that the patterning of major veins in Pilea is driven by auxin, as it is in other plants, but the altered parameters of this process make it distinct from canalization. Our model was inspired by Feugier et al.[25], who analyzed different forms of feedback between auxin flow and the polar allocation of its transporters. They showed that, if the allocation of auxin carriers in response to the auxin flux is stronger than linear (e.g., quadratic, as postulated by Mitchison[23]), the resulting feedback will lead to the formation of canals transporting auxin from sources to sinks. In contrast, if the feedback is weaker—linear or decreasing—auxin will flow away from its sources without forming canals. Weak polarization was proposed as a mechanism that positioned primordia in a model integrating phyllotaxis and vascular patterning in the shoot apical meristems of Arabidopsis[59], and as a mechanism that directed vascular strands (subsequently patterned using strong canalization) towards sinks in the meristems of Brachypodium[26]. Here we show that weak polarization by itself can pattern vascular strands as well. These strands do not connect auxin sources to sinks but divide the space between the sources, similar to how major veins partition the space between hydathodes in Pilea. We assumed the polarization model with unidirectional fluxes[60] due to its biochemical plausibility[61], and we implemented it while ignoring intercellular spaces[26] for simplicity.

The model simulates the dynamics of auxin distribution in grids of square cells. For theoretical investigations we considered 1D strands of cells and 2D rectangular grids; for the models of leaves, we clipped a 2D grid to the shape of a leaf and assumed positions of hydathodes obtained from actual leaves. Hydathodes act as the sources of auxin and, once activated, maintain constant, high auxin concentration. The concentration c_A of auxin in an arbitrary ground (non-hydathode) cell A changes according to the equation:

$$\frac{dc_A}{dt} = \sigma - \mu c_A + \sum_{B \in \mathrm{nb}_4(A)} (J_{B\to A} - J_{A\to B}), \tag{3}$$

where σ is the background rate of local synthesis of auxin, μ is the rate of auxin turnover, and $J_{B\to A}, J_{A\to B}$ represent unidirectional auxin fluxes due to its polar transport to and from cell A. These fluxes are summed over all cells B that share an edge with A, i.e., that lie in the 4-neighborhood $\mathrm{nb}_4(A)$ of A.

The unidirectional flux $J_{A\to B}$ between any pair of neighboring cells A, B is calculated as:

$$J_{A\to B} = c_A(k_d + k_p[\mathrm{PIN}]_{A\to B}), \tag{4}$$

https://doi.org/10.1038/s41467-026-71768-3

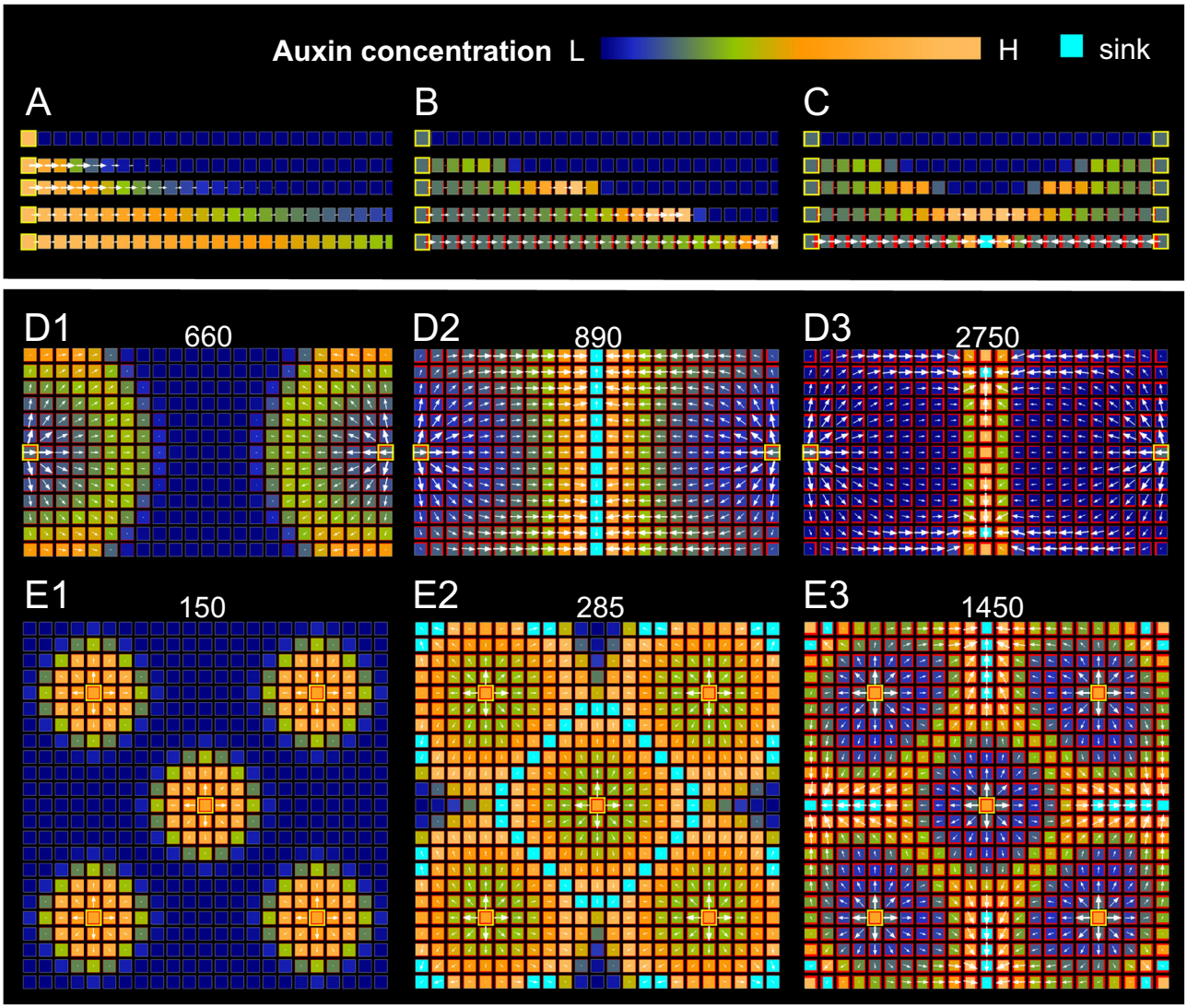

Fig. 4 | Principle of Voronoi diagram formation by the auxin-driven patterning with unidirectional fluxes. Auxin sources are highlighted by yellow boxes. Auxin concentration is indicated by the cell color. The color scheme used is indicated by a color map (top right) ranging from dark blue (low auxin, L) to pale orange (high auxin, H). Cells (sinks) that reach the maximum concentration cap, c_{max}, are colored in cyan. PIN concentration at the cell membranes is indicated by the width of red lines along the cell edges, and auxin fluxes are represented by the direction and size of white arrows. See Supplementary Table 4 for model parameters. **a** Snapshots of a simulation of pure auxin diffusion in a semi-infinite row of cells. Auxin gradually infiltrates consecutive cells without forming new maxima. **b** Same as (**a**), with polar auxin transport. An auxin maximum emerges, forming a wave that propagates away from the source. **c** Same as (**b**), in a finite-length row of cells with auxin sources at both ends. Colliding waves generate a concentration peak, which is stabilized by a concentration cap (cyan). **d** Same as (**c**), simulated on a rectangular grid with no-flux boundary conditions, and an additional cap on the rate of endocytosis. Auxin concentration waves propagate (d1) and collide half-way between the source cells (d2), forming a ridge that persist for some time after collision (d3). The numbers indicate frame numbers generated by the simulation. **e** Same as (**d**), on a square grid with 5 auxin sources. Waves of high auxin concentration collide along ridges that bisect the space between the sources, producing a Voronoi diagram.

where k_d is the rate of auxin diffusion through the wall between cells A and B (including a possible role of plasmodesmata[62]), and k_p is the rate of polar transport from A to B by PIN proteins located on the membrane of cell A abutting cell B. The abundance of this protein, $[\mathrm{PIN}]_{A\to B}$, is the net effect of PIN cycling from the cell interior to the membrane (exocytosis) and from the membrane back to the interior (endocytosis):

$$\frac{d[\mathrm{PIN}]_{A\to B}}{dt} = \alpha[\mathrm{PIN}]_{A,u}\, J_{A\to B} - \min\{\gamma[\mathrm{PIN}]_{A\to B}\, J_{B\to A}, e_{\max}\}, \qquad (5)$$

where $[\mathrm{PIN}]_{A,u}$ is the abundance of currently unallocated PIN in the interior of cell A, α is the auxin efflux-based exocytosis rate of PIN, γ is the auxin influx-based endocytosis rate, and $e_{\max}$ is the maximum endocytosis rate.

Finally, we assume that $[\mathrm{PIN}]_{A,\mathrm{total}}$, the total abundance of PIN in each cell A, is constant, thus

$$[\mathrm{PIN}]_{A,u} = [\mathrm{PIN}]_{A,\mathrm{total}} - \sum_{B\in \mathrm{nb}_4(A)} [\mathrm{PIN}]_{A\to B}. \qquad (6)$$

The operation of this model can be illustrated by a sequence of simulations, which progressively introduces different model components (Fig. 4); parameter values used in the simulations are listed in Supplementary Table 4. We first consider a one-dimensional row of cells, in which the leftmost cell has just been activated as an auxin-

producing hydathode and will maintain high constant auxin concentration throughout the simulation; the remaining ground cells have low initial concentration. With a purely diffusive transport ($k_d > 0, k_p = 0$ in Equation (4)), auxin concentration gradually increases in all ground cells, tending to the concentration of the hydathode. This process begins with the hydathode and progresses away from it (Fig. 4a). At no stage does a concentration peak emerge that could potentially trigger a localized differentiation of vascular cells. This dynamic is drastically changed in the presence of polar auxin transport ($k_p > 0$) with feedback between auxin flow and the allocation of auxin carriers. For a wide range of parameter values $\gamma \gg \alpha > 0$ (Equation (5)), a wave of high auxin concentration emerges, propagating away from the hydathode at an approximately constant speed (Fig. 4b). This emergence is not entirely surprising, as a variant of a wave associated with polar auxin transport has been reported previously in the context of a different cell polarization model[63,64]. With two hydathodes arising simultaneously, the generated waves collide, producing a maximum of auxin concentration half-way between the hydathodes (Supplementary Fig. 7a, highlighted by the yellow box). The auxin concentration in this maximum quickly rises, which reverts polarization of the adjacent cells making the maximum disappear (Supplementary Fig. 7), but it can be stabilized by various mechanisms. In the model we have imposed a cap, c_{max}, on auxin concentration (Fig. 4c); a more complex mechanism, for example involving the drainage of auxin through the petiole, may operate in actual Pilea leaves.

The generation of auxin maxima partially extends to two dimensions. In this case, wave fronts are approximately circular and collide along a linear ridge (Supplementary Fig. 8 and Supplementary Movie 1). This ridge is unstable, and even with a cap on auxin concentration, PIN quickly repolarizes away from the ridge center, redirecting auxin flow toward emerging discrete maxima (Supplementary Fig. 9 and Supplementary Movie 2). A properly chosen cap on the rate of endocytosis (parameter e_{max} in Equation (5)) significantly slows down the repolarization while preserving the preceding wave propagation and collision phases (Fig. 4d, and Supplementary Fig. 10 and Supplementary Movie 3). A more complex mechanism for introducing a saturating endocytosis rate, for example involving the CUP-SHAPED COTYLEDON2 (CUC2) protein known to control PIN reorientation in Arabidopsis leaves[65], may operate in actual Pilea leaves. In the presence of several hydathodes, the ridges form loops that surround the individual hydathodes and, with the hydathodes arising approximately at the same time, bisect the space between them (Fig. 4e and Supplementary Movie 4). The patterning process is thus an auxin-based implementation of the fundamental process generating Voronoi diagrams by colliding waves[30,66], in which hydathodes act as the polygon centers.

To examine the model's capability to simulate actual venation patterns, we digitized the contours and hydathode positions of sample Pilea leaves, and simulated the patterning process with these input data (Fig. 5a and Supplementary Movie 5; Supplementary Fig. 11 and Movies 6–9). Overlaying the resulting pattern with that of a true Voronoi diagram generated using the same hydathode positions confirmed that the auxin-driven model produced a very close approximation of a Voronoi diagram (Fig. 5b). Superimposing the generated pattern on a cleared leaf image reflected both the similarities and differences between exact Voronoi diagrams and the actual major vein patterns (Fig. 5c). To characterize them further, we divided the real leaf (Fig. 5d) and the model pattern (Fig. 5e) into three zones: peripheral (a, unshaded), where marginal secondary veins run; intermediate (b), delineated by exterior secondary veins; and central (c–e), between the midvein and lateral veins. These zones were conspicuous in both the cleared leaf and the model, and had similar shapes. In the peripheral and intermediate zones (a, b), where the hydathodes were distributed relatively regularly along the contour of the leaf edge or on the outer side of the primary vein, the polygons of the model and cleared leaves coincided closely. Larger discrepancies occurred in the central zones (c, d). Polygon boundaries did not precisely capture the course of the midvein and the geometry of the vascular pattern near the point of attachment of the leaf to the petiole, which is also consistent with our statistical tests that found more deviation from the Voronoi property near these regions (Supplementary Fig. 6). This suggests that the midvein may be patterned by a distinct process during leaf initiation, as is the case in Arabidopsis[54] and tomato[67] leaves. Moreover, throughout the leaf blade, some polygons included two or more hydathodes not separated by major veins, whereas simulated patterns adhered strictly to the Voronoi diagram (Supplementary Fig. 6). In spite of these differences, the capability of weak polarization to generate vascular patterns with loops was remarkable.

To test the robustness of the proposed patterning mechanism to variability in the initiation timing of hydathodes across the leaf blade, we simulated sequential auxin activation at hydathode positions under different spatiotemporal patterns (basipetal, centrifugal, and random; Supplementary Fig. 12). The basipetal pattern, which is consistent with tissue maturation in Pilea leaves, still produced secondary veins that closely matched an ideal Voronoi diagram, whereas centrifugal and especially random activation caused more pronounced deviations. These results indicate that as long as neighboring hydathodes activate within a similar timeframe, consistent with the spatiotemporal progression of leaf development, a Voronoi-like venation pattern robustly emerges. Thus, our proposed mechanism tolerates moderate variation in activation timing while maintaining approximate Voronoi geometry.

Experimental validation of the model

We constructed the proposed model by investigating how an auxin-driven process could produce a Voronoi pattern of veins surrounding the hydathodes. This model closely captures the patterning of secondary veins, rather than that of primary veins and minor veins, which form before and after secondary veins, respectively. To validate this model, we compared its predictions with subsequently obtained experimental data.

Gene and protein expression reporters currently used to study vein patterning in model plants (e.g., Arabidopsis and tomato) are not available for Pilea. Therefore, we performed immunoblotting and immunolocalizations with a purified anti-AtPIN serum that targets an intracellular domain in PIN proteins that is conserved in plants as different as Arabidopsis and maize (Supplementary Fig. 13, Methods). We focused on developmental stages P4-P6 (where P0 represents the youngest leaf primordium at the shoot apical meristem and larger numbers indicate progressively older primordia), during which secondary veins turn out to be patterned (Fig. 6a). Negative controls confirmed that the PIN signal, particularly around cell membranes, was not due to autofluorescence (Fig. 6b).

Key observations of PIN immunolocalization distribution. In P4 leaves, PIN signal was prominent in the midvein (Supplementary Fig. 13b). In areas around the midvein of those leaves, we observed far fewer hydathodes than in corresponding areas of P5 leaves (e.g., two hydathodes around the midvein in a representative P4 leaf vs. 9 hydathodes in corresponding areas in a representative P5 leaf). In none of the 14 P4 and P5 leaves we imaged did we observe a secondary vein without hydathodes on either side. By contrast, we observed 32 pairs of hydathodes, of which 25 had a secondary vein in between them and 7 did not.

In the epidermis of P5 leaves, PIN signal was strongest in and around hydathodes, gradually decreasing away from them (Fig. 6c1, Supplementary Fig. 13c). In the inner tissues, PIN signal was weak in hydathodes (Fig. 6c2). Around them, PIN signal was stronger, but its spatial distribution was not uniform and did not exhibit any systematic pattern. In primary veins, PIN signal remained higher than in adjacent cells (Fig. 6d). By contrast, PIN signal was weak in secondary veins at all

https://doi.org/10.1038/s41467-026-71768-3

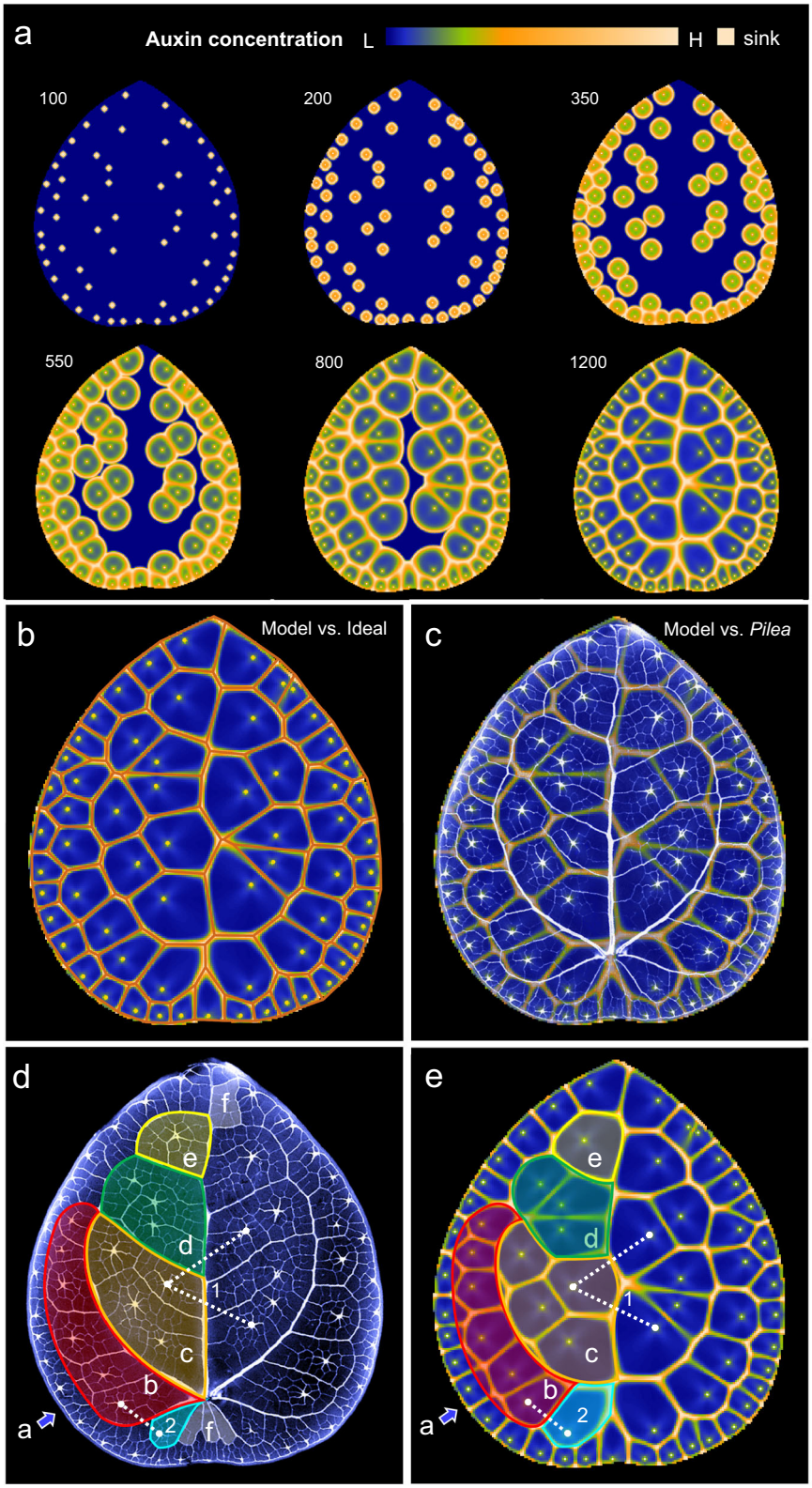

stages of their development (Fig. 6e–h). In all ground cells of P5 leaves, PIN signal was distributed uniformly along the cell outline, except in ground cells adjacent to secondary veins at later stages of their development. In those cells, PIN signal was polarly localized toward the veins (Fig. 6f, g).

In the epidermis of P6 leaves, PIN signal remained strongest in hydathodes (Fig. 6i1). In the inner tissues, PIN signal was weak in hydathodes but was strong in the circles of cells surrounding hydathodes and in emerging networks of cell files that were continuous with those cell circles (Fig. 6i2).

There were similar spatial patterns and levels of PIN expression around many pairs of adjacent hydathodes and in developing veins that almost perfectly bisected the space between the hydathodes (Fig. 6e, f). For other hydathode pairs, the vein in between was slightly

Fig. 5 | Model of auxin-driven patterning in Pilea leaves. Simulation was performed on a 200 × 220 grid of cells, clipped to the contour of an actual leaf. Hydathode positions were obtained by digitizing the leaf. **a** Snapshots of the simulation illustrating the patterning process. Wavefronts originating at the hydathodes propagate and collide, forming high-concentration ridges as in Fig. 4e. The color map indicates auxin concentration from low (L) to high (H). The numbers indicate frame numbers generated by the simulation. See Supplementary Table 4 for model parameters. **b** Overlay of the model-generated pattern (yellow) with an ideal Voronoi diagram (red) computed using hydathodes as the polygons centers. **c** Overlay of the pattern generated by the auxin-driven model and the cleared Pilea leaf. **d**, **e** Cleared and modeled leaves annotated to facilitate comparisons. a: zone on the leaf periphery; b: zone sandwiched between zone a and the primary lateral vein; **c**–**e** three conspicuous loops adjacent to the midvein; f: loops without hydathodes in the cleared leaf. Additional annotations highlight differences in vein orientation between the modeled and cleared leaves (dotted lines (1 & 2)), and differences in polygon shapes and sizes (cyan).

closer to one hydathode than the other (Fig. 6h, where the vein separating the bottom-most hydathode from the top two hydathodes is slightly closer to the periphery).

Interpretations of experimental results. The presence of the midvein before the emergence of most hydathodes and secondary veins suggests that the midvein is patterned by a separate, earlier process. This is consistent with our finding that the largest discrepancies from the Voronoi property occurred close to the primary veins. The presence of high PIN signal in the midvein suggests that its patterning may be due to canalization of auxin transport between an auxin source located near the leaf tip and an auxin sink located in the stem – as observed in previously studied model plants[54,68,69].

The presence of abundant hydathodes in P5 leaves compared to their scarcity in P4 leaves supports our assertion that hydathodes emerge approximately simultaneously. Moreover, the strong PIN signal in and around hydathodes in the epidermal layer, interpreted as indicative of high auxin concentration[70], is consistent with the postulated role of hydathodes as auxin sources. The absence of PIN signal in the inner tissues of hydathodes is surprising but does not preclude hydathodes as a source of auxin: a similar distribution has been observed in different contexts in other plants[56,57,71–73].

The absence of secondary veins without hydathodes on either side, in conjunction with the existence of hydathode pairs without a secondary vein between them, supports our assumption that hydathode development precedes that of secondary veins.

If the auxin source at hydathodes gives rise to canalization, we would expect directional differences in PIN signal strength in regions surrounding hydathodes; the absence of such directional differences supports our hypothesis that auxin transport from hydathodes is not canalized in P5 leaves. Moreover, the positions of secondary veins—which separate hydathodes rather than connecting them—and the polarization of PIN toward secondary veins in adjacent ground cells are consistent with the patterning of secondary veins by colliding waves of high auxin concentration, as postulated by our model.

The presence of many pairs of hydathodes that are nearly equidistant from the separating vein is consistent with concurrent activation of auxin sources associated with each hydathode. For other pairs (e.g., Fig. 6h), it is possible that the propagating wave from the hydathode that is further from the vein started earlier. Thus, the data include cases where nearby hydathodes appear to have been activated at the same time, as well as instances with some local asynchrony, which contributes to the approximate nature of the Voronoi diagram formed on the leaf.

We did not observe polar PIN localization in cells other than the ground cells adjacent to secondary veins. This allows for two interpretations: (i) auxin transport in Pilea leaves is generally not polar, or (ii) our immunolocalizations do not adequately capture the polar distribution of Pilea PIN1 proteins. The latter could occur because the PIN1 signal is obscured by signals from other PINs that are not polarly localized[74–76] (Supplementary Fig. 13a, western blot). As we did not detect polar PIN localization even in the midvein – where prevailing theory and data from other plants strongly indicate polarized auxin transport by PIN1—we lean toward the second interpretation.

Model review and improvements. To further verify whether the model is consistent with experimental data, we visualized the concentration of membrane-allocated PIN in the model cells (Supplementary Fig. 14b; Supplementary Movie 10). In contrast to the data, we observed high PIN concentration in the veins rather than low. To show that this discrepancy does not undermine the model's logic, we extended the model with a simple mechanism of vein differentiation (Supplementary Fig. 14c; compare with Supplementary Fig. 14a). Specifically, we assumed that (i) the cells in which auxin concentration exceeds a predefined threshold for some period of time differentiate into veins, and (ii) PIN is rapidly removed from the differentiated cells. This PIN dynamics is consistent with the PIN1 expression in all cells of incipient veins[77], and the disappearance of PIN1 from both the xylem and the phloem as the veins mature[52]. In the model, the latter process is captured by the equation

$$\frac{d[\mathrm{PIN}]_{A,\,\mathrm{total}}}{dt} = -\nu[\mathrm{PIN}]_{A,\,\mathrm{total}}, \tag{7}$$

where the parameter ν controls the removal rate.

Simulations showed that the resulting vein pattern (Supplementary Fig. 14d–f; Movies 11–13) closely resembles the pattern of auxin crests produced by the original model (Fig. 5a), but PIN concentration in the major veins is now low, in agreement with the experimental data (Fig. 6). However, in the cells surrounding the emerging veins, the concentration of membrane-allocated PIN transiently surges in a manner not observed experimentally (compare Supplementary Fig. 14f2,3 with Fig. 6e–h).

We addressed this discrepancy by incorporating an additional mechanism in the model: the dependence of PIN expression on auxin. Qualitatively, this dependence is well documented in the literature[70,78]; in the model we expressed it by controlling the PIN concentration in the ground cells (i.e., cells that do not belong to a hydathode or to a vein) using the equation

$$\frac{d[\mathrm{PIN}]_{A,\,\mathrm{total}}}{dt} = \rho \min(c_A - \delta_{min}, \delta_{max}). \tag{8}$$

The production rate ρ specifies the magnitude of the influence of auxin concentration c_A on the production or turnover of PIN in cell A, with the lower limit δ_{min} and the upper limit δ_{max}. The rate of PIN production thus changes linearly from $-\rho\delta_{min}$ for $c_A = 0$ to $\rho\delta_{max}$ for $c_A = \delta_{min} + \delta_{max}$.

The postulated interactions between auxin, PIN and vein differentiation are summarized in Fig. 7a and are further illustrated in Fig. 7c–e (Movies 14–20, Supplementary Table 5 for model parameters). The resulting pattern of differentiated veins (Fig. 7b, Supplementary Movie 14) continues to closely match the Voronoi pattern of auxin crests produced by the original model (Fig. 5). As in the intermediate model without auxin-controlled PIN production (Supplementary Fig. 14c–f), PIN concentration in the differentiated veins drops to zero; however, in contrast to the intermediate model, there are no transient surges of membrane-allocated PIN concentration in the cells adjacent to the veins. In further agreement with experimental data, the concentration of membrane-allocated PIN in the hydathodes

https://doi.org/10.1038/s41467-026-71768-3

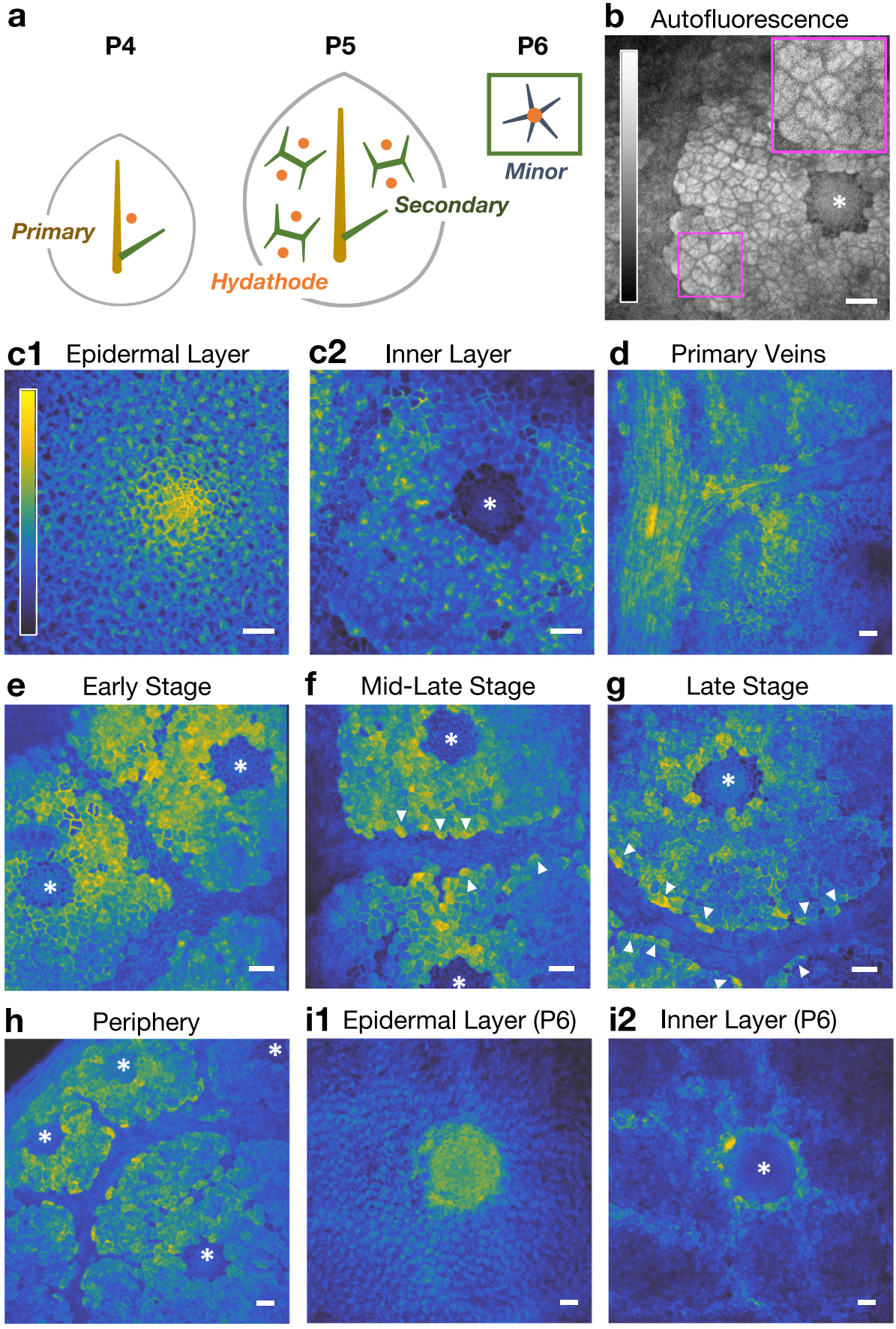

Fig. 6 | PIN immunolocalization in developing Pilea leaves. a Schematic of Pilea leaf development from P4 to P6, highlighting the order in which primary veins, hydathodes, secondary veins, and minor veins form. **b** Autofluorescence signal in a P5 leaf including a secondary vein (to the left) and a hydathode (asterisk). The look-up table (LUT) ramp visualizes the 1–99% signal intensity range. Inset: 1.75 × magnification of the boxed region. Representative example of three independent experiments. **c** PIN signal in a region of a P5 leaf surrounding a hydathode. (c1) Epidermal layer showing strong PIN signal in and surrounding the hydathode. LUT ramp, also applied to all successive images, visualizes the full range of maximum-projected signal intensity. (c2) Inner layer showing weak PIN signal in the hydathode (asterisk). A secondary vein is forming to the left. **d** Inner layer of a P5 leaf showing PIN signal in the midvein. **e**–**g** Progression of secondary vein formation in P5 leaves (asterisks denote hydathodes). **e** Early stage: In vein cells that have yet to differentiate, PIN signal is weak and isotropically localized at the cell outline. In ground cells, PIN signal is also mainly isotropic but stronger than in vein cells. **f** Mid-Late stage: In vein cells that have started to differentiate, PIN signal falls below detection levels. In ground cells adjacent to a forming secondary vein, PIN signal at the cell outline becomes polarized toward the forming vein (arrowheads). **g** Late stage: All vein cells have differentiated and show no detectable PIN signal. PIN polarity in adjacent ground cells persists toward the forming vein (arrowheads). **h** Peripheral region of a late-stage P5 leaf showing differentiated transverse and perimarginal secondary veins with no detectable PIN signal in veins or hydathodes (asterisks). **i** P6 leaf. (i1) Epidermal layer showing PIN signal in the hydathode. (i2) Inner layer with no PIN signal in the hydathode (asterisk). Bright cell files around the hydathode form a net-like pattern of minor veins. Scale bars: 20 μm.

is smaller than in the rings of cells immediately surrounding them, and gradually decreases further away from the hydathodes. The improved colliding wave model of secondary vein formation in Pilea is thus consistent with the immunolocalization data.

Discussion

Reticulate leaf venation patterns, defined by the presence of loops, are ubiquitous in flowering plants, yet their geometry has so far eluded concise characterization. We have shown that the patterns of major veins in Pilea leaves approximate Voronoi diagrams, with hydathodes acting as the Voronoi polygon centers. Given the diverse and complex reticulate vascular patterns observed in nature, it was unexpected to find an example where the pattern can be explained by such a simple geometric principle.

We have also proposed and modeled a biologically plausible mechanism approximating the observed patterns. Similar to canalization, which has dominated the understanding of vascular patterning in plants for the last 50 years, our model attributes the patterning of veins in Pilea leaves to auxin. Canalization, however, creates channels of high auxin flux that connect auxin sources to sinks, and these channels primarily form open, tree-like vascular patterns. By contrast, our model generates auxin concentration waves that propagate away from hydathodes and form crests upon colliding. These crests pattern vascular strands that assemble into closed loops surrounding each hydathode, thus tessellating the leaf surface into Voronoi polygons.

Our model has led to predictions, which we have tested experimentally by visualizing the distribution of PIN proteins at key stages of Pilea leaf venation patterning. With relatively minor adjustments, we obtained remarkable agreement of the model with the observations. Our results also suggest topics deserving further exploration.

Patterning of primary veins. Our model generates veins that approximately coincide with the primary veins patterned by hydathodes. Nevertheless, experimental data indicate that primary veins appear before hydathodes and are patterned by a separate mechanism (canalization). The inclusion of this mechanism may improve the agreement of the model with experimental observations near the midvein and the attachment point to the petiole, where the discrepancies in the shapes and sizes of model-generated polygons vs. the vascular polygons in Pilea are significant (Fig. 5c and Supplementary Fig. 6; Supplementary Note 4).

Patterning of hydathodes. Across leaves, hydathodes appear at relatively similar locations on the leaf blade (Fig. 3c), suggesting that hydathode placement is under control of a regulated patterning mechanism. Uncovering the function that characterizes the spatial distribution of hydathodes, along with its underlying placement mechanism, would lead to a more comprehensive understanding of Pilea leaf patterning.

Patterning of minor veins. Experimental results demonstrate the emergence of minor veins that connect hydathodes to major veins, suggesting a canalization process, with hydathodes acting as auxin sources and major veins acting as auxin sinks. Patterning processes combining weak and strong polarization have been proposed[26,59], and it is possible that such integration also plays a role in the patterning of minor veins in Pilea leaves.

The impact of growth on patterning. Our model was constructed using the simplifying assumption that leaf size and shape were fixed. Future models may shed light on the degree to which leaf growth affects the process of Voronoi pattern formation.

Concluding remarks. Our model may extend to reticulate patterning in other species with laminar hydathodes, where major veins surround hydathodes and connect to them via minor veins. Examples include *Ficus formosana*[79], *Ficus diversifolia*[80], and many other species in *Urticaceae*, the nettle family, to which Pilea belongs[81]. While the reticulate venation patterns found in these species visually appear to adhere to the Voronoi geometry less strictly than in Pilea, it would be interesting to examine if the wave collision mechanism suggested by our model can generate these patterns by varying parameters, such as the timing of auxin production in the hydathodes, and by considering growth patterns of these leaves. For species with reticulate veins that lack laminar hydathodes, it is possible that auxin is synthesized at discrete sites distributed over the leaf blade, serving an analogous role to the hydathodes[82]. Because weak polarization of auxin transport is not limited to Pilea[26], the combination of weak polarization and distributed local auxin maxima may be a more widespread mechanism of reticulate pattern formation[23,83–87].

It is still not known whether a Voronoi-like relationship between hydathodes and major veins offers any functional benefits compared to alternative network patterns. Computational modeling may help decipher the trade-offs that occur between different patterns in different environments in terms of hydraulic balance[11,38,88,89], structural support[90], and network robustness[19].

Research on pattern formation has for a long time been dominated by Turing's reaction-diffusion model[7,91–93] and Wolpert's positional information model[94–96]. By contrast, in plants, vein patterning is controlled by a different mechanism, based on active transport and facilitated diffusion, rather than passive diffusion[68,74,97–99]. Although more mathematical work is needed to analyze the breadth of patterns this mechanism can generate, our model of vascular pattern formation in Pilea adds to the already rich tapestry of auxin-driven models.

Methods

Pilea growth conditions

Pilea plants were purchased from Hicks Nursery, Garden City, NY. Plants were propagated by the provider (Harster Greenhouse, CA) by selecting and raising the strongest runners in the generation every 6 months, and were purchased at relatively the same age. Upon arrival, plants were grown in 6-inch pots in an indoor environment with low indirect light. Plants grown in these indoor conditions were used in the initial Voronoi I, II, and III tests ($n = 34$ leaves from 6 plants), and were used as the control in the stress experiments. Plants used for stress treatments stayed in the indoor condition for at least 1 week before the treatments started.

https://doi.org/10.1038/s41467-026-71768-3

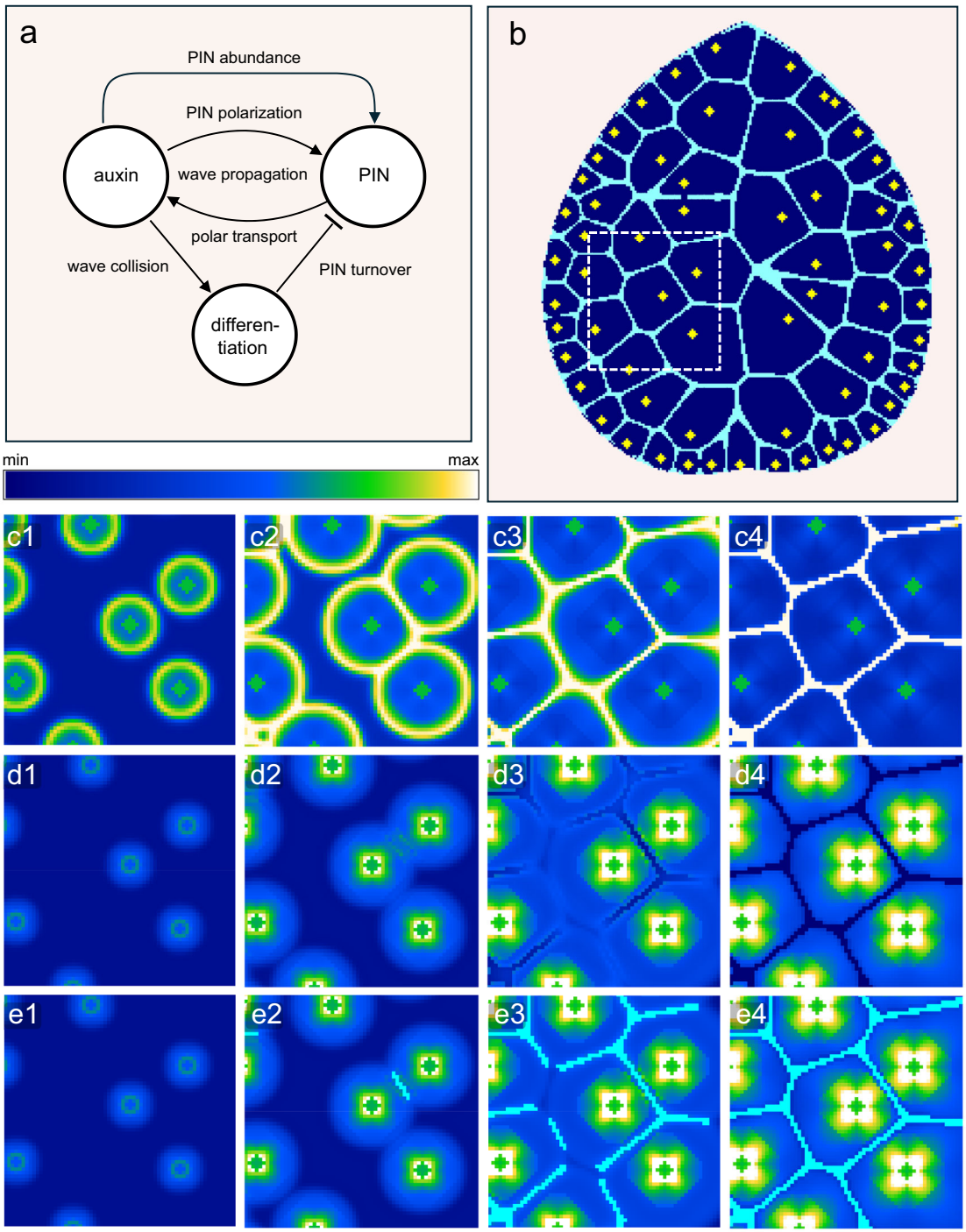

Fig. 7 | Improved model of vein patterning in Pilea leaves. a Schematic of the interaction between auxin, PIN, and vein differentiation. **b** The resulting pattern of differentiated veins (cyan) generated by the model after 750 simulation steps. **c**–**e** Progression of auxin concentration (**c**), membrane PIN concentration (**d**), and vein differentiation superimposed on membrane PIN concentration (**e**) in the leaf region highlighted in panel (**b**). Columns 1 to 4 represent simulation states after 190, 300, 450 and 650 steps. The feedback between auxin propagation and PIN polarization creates waves of high auxin concentration propagating away from the hydathodes (**c**, **d**). Colliding waves create crests that trigger vein differentiation (**e**) and PIN turnover, which results in low PIN concentration in differentiated veins (d4). Minimal or absent surges in membrane PIN concentration in non-differentiated cells surrounding the veins (d3, e3) and low concentration of PIN away from the hydathodes in later stages of patterning (d4, e4) are due to the control of PIN expression by auxin.

For the stress treatments, we exposed 6 Pilea plants in each of three conditions, namely shade (22 °C, R:FR = 0.4, PPFD = 45), high-light intensity (22 °C, PPFD = 55–65), and high-temperature (30 °C, PPFD = 55), for 5 weeks. Plants in stress conditions were grown on a long-day cycle with 16hr light (7 AM to 11 PM) and 8hr dark in growth chambers. Shade and control plants were irrigated with 250 ml water once per week; high-light and high-temperature plants were watered twice every week to keep the soil at the same approximate water level (See Supplementary Table 6 for treatment condition details). Plants were then shifted to non-stress indoor conditions for 1 week, and the emerging leaves that had developed during the stress treatment were collected for analysis.

Leaf clearing, staining, and imaging

Fresh leaves were phenotyped with a stereo microscope (Zeiss Stemi 508). Each individual leaf was mounted on a customized transparent acrylic platform and laid flat by a covering acetate sheet. For each leaf, multiple, high-resolution micrographs were taken (Zeiss, Axiocam 208, Color) with the abaxial side up and planarly stitched together with software (Panorama Stitcher v1.11.1).

To image the vein architecture in cleared leaves, we followed the clearing and staining protocol for studies of leaf architecture[100]. Briefly, fresh Pilea leaves were first immersed in Histoclear for 1 hr to remove the cuticle, and then immersed in 5% NaOH solution at 37 °C for 48 hrs in Petri dishes, with one change of solution at 24 hrs. The leaves were then bleached with sodium hypochlorite (3%) until transparent (2-4 hrs, depending on leaf size). Leaves were then rinsed in distilled water, then dehydrated with 30%, 50%, 70%, 90%, and 100% ethanol for 30 minutes each at room temperature. Cleared leaves were then placed in 0.5% safranin in 100% ethanol for staining overnight. Destaining was done by rinsing the leaf specimen in 100% ethanol and acidifying it with 3-6 drops of 6M hydrochloric acid until the mesophyll tissues appeared pale white. Leaves were rehydrated with 90%, 70%, 50%, 30%, and 10% ethanol for 30 min each at room temperature. Finally, the leaves were mounted in a 10% glycerol medium and scanned with a flat-bed scanner (Epson Perfection V600).

Tracing of major veins and hydathodes

Tracing was performed on the stitched light microscopy images using a digitizing tablet (Wacom Cintiq Pro 16) and commercial graphics software (SketchbookPro 8.8.5). We formulated tracing rules for the major veins based on Pilea's *brochidodromous* vein architecture[40], which means that the major veins form loops with locally consistent widths and do not end in the parenchyma cells.

Major vein tracing rules: We traced veins segment by segment. A segment is a relatively straight piece of vein connected by other veins (major or minor) on both ends. Major veins were segments that have consistent widths and are at least 1.5 times the width of the minor veins that they directly connect to. We also required all major veins to end at a junction with other major veins, to ensure all major veins are part of a closed loop.

Hydathode tracing rules: Two observations were used to distinguish hydathodes from ground tissue. First, hydathodes are densely packed with cells, which makes them appear less transparent than ground tissues. Second, in mature leaves, hydathodes are anatomically located at minor vein junctions and can be clearly seen as having star-shaped connections to minor veins (Supplementary Fig. 1). Based on the two observations, we identified the "shadowy dots" that connect to ≥4 minor veins as hydathodes.

Tracing of veins and hydathodes was performed by a single researcher and then reviewed and subsequently edited by two other researchers until consensus was reached (see Supplementary Fig. 1 for examples superimposed with the microscopy images). Traced images were stored as PSD files and layers were output to vector formats. We used NEFI[101], an OpenCV-based network extraction pipeline, to convert the vein tracing to an undirected planar graph, where edges (vein segments) and nodes (junctions and connections of vein segments) were defined from the skeleton of the tracing pattern. Hydathode location extraction was performed with custom code (Python 3.8) by finding the center of the traced points. The extracted vein graph (edges and nodes for vein segments) and hydathodes (a node set of hydathode positions) were then stored together as an undirected graph object in NetworkX (2.7.1, a Python library, for studying graphs and networks) under the same coordinate system.

Bayesian generalized linear mixed-effects models

We collected multiple leaves from each Pilea plant, which introduced a possible statistical dependency for leaves from the same plants. To control for the random effects from plants when calculating performance differences between hydathodes and reference point sets for our statistical tests, we used linear mixed-effect regression models. For discrete hydathode counts data, we used Poisson mixed-effect regression models.

All mixed-effects models were fitted in a Bayesian hierarchical framework using the Bayesian Model-Building Interface (Bambi 0.9.1[102]). Bambi generates weakly informative priors for all model variables and uses a Hamiltonian Monte Carlo algorithm to draw from the posterior distributions. For each model between a treatment group (in our case, a different point set, or a stress condition) and the control, we used 5 independent chains of 2000 draws, and we recorded the fraction of total draws that lie between 50% to 100% (the probability of direction, p_d). The variable p_d is an index of effect that represents the certainty with which an effect goes in a particular direction, either positive or negative[103]. We calculated $(1 - p_d)$ as the p-value to test statistical significance.

Detailed methods for the Voronoi I, II, and III tests

Voronoi I: Quantifying local deviation. Proof for the perpendicular bisection corollary of Voronoi centers and edges can be found in Green and Sibson (1978)[104]. When two vein polygons share two or more edges instead of one, we picked a random edge among all edges to be tested.

Voronoi II: Jaccard similarity. The Jaccard index measures the proportional area overlap between corresponding polygons of two tessellations, and it offers a unitless and interpretable measure of the alignment between the two tessellations. We computed the J-index between the Voronoi polygons generated using hydathodes as centers and the actual major vein polygons in Pilea leaves. For this test, we used the full set of hydathodes on the leaf as centers, including both single-polygon hydathodes and multi-polygon hydathodes (hydathodes in polygons that enclose more than one hydathode). We also computed the J-indices between the Voronoi polygons generated using the reference point sets as centers and the actual major vein polygons in Pilea leaves. For these tests, we generated the reference points in only single-hydathode polygons. For multi-hydathode polygons, we fixed the reference points to the locations of the actual hydathodes. This was done for two reasons: (a) so that the the number of centers (and hence, the number of polygons) was the same across all comparisons; and (b) so that the influence of multi-hydathode polygons towards the J-index was equal for all comparisons.

White-noise distorted Voronoi diagrams: We used the J-index between the white-noise distorted Voronoi diagrams and the exact Voronoi diagrams to estimate the magnitude of mismatch between Pilea major veins and the exact Voronoi diagram. Voronoi diagrams were computed with the hydathode sets of a leaf sample as the Voronoi centers. Then for each Voronoi vertex, we added a vector of fixed length pointing to a random direction to distort the perfect Voronoi diagram and create a "noisy" version of the exact polygons. We explored noise levels ranging from 1% to 20% the length of the mean polygon axes added to the vertices. For each distorted Voronoi diagram, we applied the Voronoi II test with the exact Voronoi diagram and recorded their J-indices (Supplementary Fig. 2a, b).

Mean-split *k-d* tree algorithm: To create an alternative tessellation to test polygon overlap, we modified the *k-d* tree algorithm[105], which is a space-partitioning data structure, to create a spatial subdivision that: 1) recursively forms bisections with point sets, and 2) is produced hierarchically. In 2D, given a set of points as input, the algorithm recursively finds a partition for the point set with one dimension fixed, and the partition of the other dimension is calculated to be the averaged coordinates of all points in the split zone (Supplementary Fig. 2c). For Pilea, we started with splitting all hydathodes in the direction parallel to the midvein. In each step, we iteratively used either the parallel or perpendicular direction to subdivide the point

sets, until all partitions contain only one hydathode (Supplementary Fig. 2d).

Voronoi III: Center prediction. We used the corollary of Voronoi property to solve for the best-predicted center coordinates given the polygon edges[47].

Given two adjacent polygons, P_l and P_m with a common edge E_i, the predicted Voronoi centers of P_l and P_m are at $(\hat{x}_l, \hat{y}_l)$ and $(\hat{x}_m, \hat{y}_m)$. The two end vertices of E_i are (u_p, v_p) and (u_q, v_q). Let E_i be a segment of the line defined by $y = s_i x + b_i$, where

$$s_i = (v_p - v_q)/(u_p - u_q) \quad b_i = s_i u_p - v_p \tag{9}$$

To form a linear system, we will express the Voronoi centers with the geometric relationship in the corollary. The condition on the slope gives:

$$(\hat{x}_l/s_i) + \hat{y}_l - (\hat{x}_m/s_i) - \hat{y}_m = 0 \tag{10}$$

The condition of distance equality gives

$$s_i\hat{x}_l - \hat{y}_l + s_i\hat{x}_m - \hat{y}_m = -2b_i \tag{11}$$

For a tessellation with k interior edges and n polygons, Eqs. (10) and (11) for all edges together give a system of $2k$ equations with $2n$ unknowns. In ideal Voronoi diagrams, the average number of edges per Voronoi polygon is about 6[28], therefore $2k < 2n$. Because this test assumes each polygon has exactly one center, we removed from analysis all Pilea polygons that contained more than one hydathode. Furthermore, considering a dual graph where nodes are polygons and edges exist between adjacent polygons, we only applied this test to the set of polygons in the largest connected component of this graph. This was done to ensure that there were enough constraints in the system of equations such that the system was not under-determined. Specifically, using the set of polygons in the largest connected component, we found that 33 out of the 34 control samples were over-determined, and hence, we could solve for unique Voronoi center locations by minimizing the ℓ_2 error.

Unlike ideal Voronoi diagrams, the traced Pilea vein polygons from tracing sometimes share multiple edges. In such cases, we aimed to find the solution that results in the least distance error with the testing point set (e.g., hydathodes). However, the number of linear systems to select to solve for grows exponentially with the number of polygon pairs that share multiple edges. The heuristic that we adopted for the Pilea leaf graphs was to repeatedly pick random edge combinations 100 times the number of polygon pairs, and report the best solution among them. The resulting error is on average 97.8 ± 0.7% of the global best solution, computed using brute force on one leaf sample tested, and it performs much better than greedily selecting the best edge (local minimum).

Sample alignment

To analyze the hydathode distribution from multiple samples, we performed an Ordinary Procrustes style analysis on 32 leaves (8 samples, from each of the 4 environmental conditions). We aligned all samples in the same orientation and scaled by performing isomorphic transformations. The 8 samples we used from each condition were 4 leaves from 2 plants, rather than a random sampling from all leaves, to reduce the variation introduced to the alignment. For every sample, we select the petiole node (P) and the furthest intersection node (Q) where the primary veins meet as two landmark points. By rotating and scaling the line segment PQs of all samples to exact alignment, we reach reasonable superimposition of the leaf graphs, and the hydathode distribution shows a clear spatial pattern, with higher density between the primary and secondary veins that originate from the petiole, and between secondary veins and the leaf boundary (Fig. 3c).

Protein extraction and immunoblotting

Approximately 50 mg of P5 leaves from *Pilea peperomioides* and *Arabidopsis thaliana* were harvested, flash frozen in liquid nitrogen, and stored at −80 °C until use. For Pilea, leaves were ground in liquid nitrogen using a chilled mortar and pestle. Ground leaves were homogenized and proteins were extracted with 3 mL of extraction buffer (0.1 M Tris-HCl, pH 8.0, 0.01 M $MgCl_2$, 18% [w/v] sucrose, 40 mM β-mercaptoethanol, 2% SDS) per gram of ground tissue. Extracts were filtered through Miracloth (Millipore, catalog no. 475855-1R) and centrifuged at 14, 000 × g for 15 min at 4 °C, followed by addition of 2 × urea buffer (120 mM Tris-HCl, pH 6.8, 4% SDS, 20% glycerol, 0.02% bromophenol blue, 10% β-mercaptoethanol, 8 M urea) and incubation at RT for 5 min. For *Arabidopsis*, microsomal proteins were isolated with minor modifications from Pedmale et al. (2007)[106]. Briefly, *Arabidopsis* leaves were homogenized in ice-cold buffer containing 25 mM MOPS-NaOH (pH 7.8), 250 mM sucrose, 0.1 mM $MgCl_2$, 8 mM cysteine, 10 mM NaF, and 1 × ProBlock™ Gold Plant Protease Inhibitor Cocktail (GoldBio, catalog no. GB-332-1). The homogenate was subjected to ultracentrifugation at 100, 000 × g for 1 h to isolate microsomal pellets. These microsomal fractions were then resuspended in a buffer composed of 5 mM potassium phosphate (pH 7.8), 250 mM sucrose, 4 mM KNO_3, and 1 × ProBlock™ Gold Plant Protease Inhibitor Cocktail, using a Dounce homogenizer. For both species, 25 μL of total protein extract was resolved on 10% SDS-PAGE gels at 130 V for 1.5 h and transferred to PVDF membranes (Merck Millipore, catalog no. PFL00010) using electroblotting. An equivalent amount of total protein was resolved on a parallel gel, which was stained with Coomassie Blue and used as a loading control. Membranes were blocked for 1 h at RT in TBST buffer (20 mM Tris-HCl, pH 7.6, 137 mM NaCl, 0.05% Tween-20) supplemented with 5% [w/v] BSA and incubated overnight at 4 °C with anti-PIN antibody[107] (1:100 dilution in TBST buffer supplemented with 1% BSA). Membranes were washed three times in TBST buffer and incubated with HRP-conjugated anti-rabbit secondary antibody (BioRad, catalog no. #1706515) (1:10,000 dilution in TBST buffer supplemented with 1% BSA). After three washes in TBST buffer, proteins were detected by chemiluminescence.

Immunolocalization and microscopic analyses of PIN proteins in Pilea leaves

Primordia were staged by visual inspection under a dissecting stereomicroscope at 5 × magnification, with P0 designated as the youngest visible primordium initiating at the flank of the shoot apical meristem. PIN proteins were detected in Pilea P4–P6 leaves using a modified immunolocalization protocol[108]. Briefly, freshly harvested leaves from independent replicates were rinsed with distilled water and fixed in 100% methanol at 37 °C for 20 min. Leaves were then transferred to 800 μL of fresh methanol and gradually rehydrated to 20% methanol at 60 °C by the addition of 200 μL distilled water every 2 min for 40 min. Leaves were mounted briefly on glass slides preloaded with 60 μL of water for washing, and water was blotted off from the leaves, which were then transferred into a 24-well plate for subsequent treatments. Cell walls were digested by incubating each leaf in 100 μL of enzyme solution (0.2% Driselase (Sigma, catalog no. D9515-1G) and 0.15% Macerozyme (Phytotech, catalog no. M481) in 2 mM MES, pH 5.0) at 37 °C for 30–40 min, followed by washing with 100 μL of 1 × MTSB (500 mL: 7.5 g PIPES, 0.85 g EDTA, 0.61 g $MgSO_4 \cdot 7H_2O$, 1.25 g KOH, pH 6.9). Membranes were permeabilized with 100 μL of 3% IGEPAL C630 and 10% DMSO in 1 × MTSB for 15–20 min at 37 °C. Leaves were washed four times with 1 × MTSB (3 min each). Leaves were blocked by incubating in 60 μL of 5% BSA in 1 × MTSB for 20 min at RT with gentle agitation. Primary antibody incubation was performed with rabbit anti-PIN1[107] (1:100) in 1 × MTSB for 2 h at 37 °C, followed by three washes in 1 × MTSB (5 min each). Secondary detection was carried out with Alexa Fluor™ 594-conjugated goat anti-rabbit IgG cross-adsorbed (2 μg/mL; Thermo Fisher, catalog no. A-11012) for 1 h at 37 °C. Samples

were washed as above and mounted in VECTASHIELD Antifade mounting medium (H-1000-NB; Vector Laboratories). Imaging was performed using a 40 × objective of a Zeiss LSM 900 confocal microscope at 0.5 × and 1 × zoom values. PIN1 fluorescence was detected using 561 nm excitation and 580–700 nm emission (Alexa Fluor™ 594 channel). Autofluorescence was simultaneously captured using 488 nm excitation and 561–700 nm emission. Z-stacks were acquired for all the images.

Image processing and visualization

Images were visualized in FIJI[109] and processed in Python to generate figures. To correct for uneven orientation of young leaves, some image stacks were rotated using `scipy` (Python). Maximum-intensity projections were generated through slices capturing either the epidermal or inner cell layer. For display, pixel intensities were linearly rescaled to the 0-1 range.

For autofluorescence controls, where overall signal was low, the 1st and 99th percentiles of pixel intensity were used as lower and upper bounds, respectively, to reduce the influence of spurious noise. For the radial 1D intensity profile (Supplementary Fig. 13c), pixel intensities within concentric rings up to a radius of 75 μm from the hydathode center were averaged to obtain an azimuthal (radial) profile. The resulting mean intensity values were mirrored to display a symmetric curve from $-r$ to $+r$, with shaded regions representing bootstrap-derived 95% confidence intervals.

Reporting summary

Further information on research design is available in the Nature Portfolio Reporting Summary linked to this article.

Data availability

The processed data used for statistical analyses are available on GitHub at (https://github.com/cici-xingyu-zheng/VoronoiVein). Source data are provided with this paper.

Code availability

Code for the Voronoi statistical tests is available on GitHub at (https://github.com/cici-xingyu-zheng/VoronoiVein). Code for the computational models is available on GitHub at (https://github.com/AlgorithmicBotany/pilea-voronoi). Computational models were written in C++ extended with constructs of the L+C plant modeling language[110] and executed using the `LPFG` simulator incorporated into the Virtual Laboratory (`vlab`) v.5.0 modeling environment available on GitHub at (https://github.com/AlgorithmicBotany/vlab).

References

1. Ball, P. et al. *The Self-made Tapestry: Pattern Formation in Nature* https://books.google.com/books?id=Fz1RAAAAMAAJ (Oxford University Press, 2001).
2. West, G. B., Brown, J. H. & Enquist, B. J. A general model for the origin of allometric scaling laws in biology. *Science* **276**, 122–126 (1997).
3. West, G.*Scale: The Universal Laws of Life, Growth, and Death in Organisms, Cities, and Companies* https://books.google.com/books?id=bJPZDAAAQBAJ (Penguin Publishing Group, 2017).
4. Mandelbrot, B.*The Fractal Geometry of Nature*. Einaudi paperbacks https://books.google.com/books?id=0R2LkE3N7-oC (Henry Holt and Company, 1983).
5. Meinhardt, H. et al. *The Algorithmic Beauty Of Sea Shells*. (Springer Science & Business Media, 2009).
6. Hotton, S. et al. The possible and the actual in phyllotaxis: bridging the gap between empirical observations and iterative models. *J. Plant Growth Regul.* **25**, 313–323 (2006).
7. Kondo, S. & Miura, T. Reaction-diffusion model as a framework for understanding biological pattern formation. *science* **329**, 1616–1620 (2010).
8. Prusinkiewicz, P., Lindenmayer, A. & Hanan, J.*The Algorithmic Beauty of Plants*. Virtual laboratory https://books.google.com/books?id=deIPAQAAMAAJ (Springer-Verlag, 1990).
9. Bohn, S., Andreotti, B., Douady, S., Munzinger, J. & Couder, Y. Constitutive property of the local organization of leaf venation networks. *Phys. Rev. E* **65**, 061914 (2002).
10. Perna, A., Kuntz, P. & Douady, S. Characterization of spatial networklike patterns from junction geometry. *Phys. Rev. E* **83**, 066106 (2011).
11. McKown, A. D., Cochard, H. & Sack, L. Decoding leaf hydraulics with a spatially explicit model: principles of venation architecture and implications for its evolution. *Am. Naturalist* **175**, 447–460 (2010).
12. Blonder, B., Violle, C., Bentley, L. P. & Enquist, B. J. Venation networks and the origin of the leaf economics spectrum. *Ecol. Lett.* **14**, 91–100 (2011).
13. Blonder, B. et al. Linking functional traits to multiscale statistics of leaf venation networks. *N. Phytol.* **228**, 1796–1810 (2020).
14. Katifori, E. & Magnasco, M. O. Quantifying loopy network architectures. *PloS one* **7**, e37994 (2012).
15. Mileyko, Y., Edelsbrunner, H., Price, C. A. & Weitz, J. S. Hierarchical ordering of reticular networks. *PloS one* **7**, e36715 (2012).
16. Ronellenfitsch, H., Lasser, J., Daly, D. C. & Katifori, E. Topological phenotypes constitute a new dimension in the phenotypic space of leaf venation networks. *PLoS Comput. Biol.* **11**, e1004680 (2015).
17. Rolland-Lagan, A.-G., Amin, M. & Pakulska, M. Quantifying leaf venation patterns: two-dimensional maps. *Plant J.* **57**, 195–205 (2009).
18. Roth-Nebelsick, A., Uhl, D., Mosbrugger, V. & Kerp, H. Evolution and function of leaf venation architecture: a review. *Ann. Bot.* **87**, 553–566 (2001).
19. Katifori, E., Szöllősi, G. J. & Magnasco, M. O. Damage and fluctuations induce loops in optimal transport networks. *Phys. Rev. Lett.* **104**, 048704 (2010).
20. Sachs, T. Polarity and the induction of organized vascular tissues. *Ann. Bot.* **33**, 263–275 (1969).
21. Sachs, T. The control of the patterned differentiation of vascular tissues. In *Advances in botanical research*, **9**, 151–262 (Elsevier, 1981).
22. Sachs, T. et al. *Pattern Formation In Plant Tissues*. (Cambridge University Press, 1991).
23. Mitchison, G. A model for vein formation in higher plants. *Proc. R. Soc. Lond. Ser. B. Biol. Sci.* **207**, 79–109 (1980).
24. Rolland-Lagan, A.-G. & Prusinkiewicz, P. Reviewing models of auxin canalization in the context of leaf vein pattern formation in Arabidopsis. *Plant J.* **44**, 854–865 (2005).
25. Feugier, F. G., Mochizuki, A. & Iwasa, Y. Self-organization of the vascular system in plant leaves: inter-dependent dynamics of auxin flux and carrier proteins. *J. Theor. Biol.* **236**, 366–375 (2005).
26. O'Connor, D. L. et al. A division in PIN-mediated auxin patterning during organ initiation in grasses. *PLoS Comput. Biol.* **10**, e1003447 (2014).
27. Haskovec, J., Jönsson, H., Kreusser, L. M. & Markowich, P. Auxin transport model for leaf venation. *Proc. R. Soc. A* **475**, 20190015 (2019).
28. Okabe, A., Boots, B., Sugihara, K. & Chiu, S.*Spatial Tessellations: Concepts and Applications of Voronoi Diagrams*. Wiley Series in Probability and Statistics https://books.google.com/books?id=jRjvAAAAMAAJ (Wiley, 2000).

29. Aurenhammer, F. Voronoi diagrams—a survey of a fundamental geometric data structure. *ACM Comput. Surv. (CSUR)* **23**, 345–405 (1991).
30. Aurenhammer, F., Klein, R. & Lee, D.-T.*Voronoi diagrams and Delaunay triangulations* (World Scientific Publishing Company, 2013).
31. Imelińska, C., Downes, M. & Yuan, W. Semi-automated color segmentation of anatomical tissue. *Comput. Med. Imaging Graph.* **24**, 173–180 (2000).
32. Khiripet, N., Khantuwan, W. & Jungck, J. R. Ka-me: a Voronoi image analyzer. *Bioinformatics* **28**, 1802–1804 (2012).
33. Sánchez-Gutiérrez, D. et al. Fundamental physical cellular constraints drive self-organization of tissues. *EMBO J.* **35**, 77–88 (2016).
34. Jungck, J. R., Pelsmajer, M. J., Chappel, C. & Taylor, D. Space: The re-visioning frontier of biological image analysis with graph theory, computational geometry, and spatial statistics. *Mathematics* **9**, 2726 (2021).
35. Koch, A. & Meinhardt, H. Biological pattern formation: from basic mechanisms to complex structures. *Rev. Mod. Phys.* **66**, 1481 (1994).
36. Hoffmann, J., Donoughe, S., Li, K., Salcedo, M. K. & Rycroft, C. H. A simple developmental model recapitulates complex insect wing venation patterns. *Proc. Natl. Acad. Sci.* **115**, 9905–9910 (2018).
37. Radcliffe-Smith, A. 5. pilea peperomioides: Urticaceae. *The Kew Magazine* 14–19 (1984).
38. Cerutti, A. et al. Mangroves in the leaves: anatomy, physiology, and immunity of epithemal hydathodes. *Annu. Rev. Phytopathol.* **57**, 91–116 (2019).
39. Paauw, M. et al. Hydathode immunity protects the arabidopsis leaf vasculature against colonization by bacterial pathogens. *Curr. Biol.* **33**, 697–710 (2023).
40. Ellis, B. et al. *Manual of leaf architecture* (Cornell University Press, 2009).
41. Suzuki, A. & Iri, M. Approximation of a tessellation of the plane by a voronoi diagram. *J. Oper. Res. Soc. Jpn.* **29**, 69–97 (1986).
42. Faisal, T. R., Hristozov, N., Rey, A. D., Western, T. L. & Pasini, D. Experimental determination of philodendron melinonii and arabidopsis thaliana tissue microstructure and geometric modeling via finite-edge centroidal voronoi tessellation. *Phys. Rev. E* **86**, 031921 (2012).
43. Bohn, S., Douady, S. & Couder, Y. Four sided domains in hierarchical space dividing patterns. *Phys. Rev. Lett.* **94**, 054503 (2005).
44. Bohn, S., Pauchard, L. & Couder, Y. Hierarchical crack pattern as formed by successive domain divisions. *Phys. Rev. E* **71**, 046214 (2005).
45. Laguna, M. F., Bohn, S. & Jagla, E. A. The role of elastic stresses on leaf venation morphogenesis. *PLoS Comput. Biol.* **4**, e1000055 (2008).
46. Dierking, I., Flatley, A. & Greenhalgh, D. Voronoi patterns in liquid crystal textures. *Journal of Molecular Liquids* 116553 (2021).
47. Evans, D. G. & Jones, S. M. Detecting Voronoi (area-of-influence) polygons. *Math. Geol.* **19**, 523–537 (1987).
48. Perrin, A. et al. *Contribution à l'étude de l'organisation et du fonctionnement des hydrathodes: recherches anatomiques ultrastructurales et physiologiques* (Université Claude Bernard, 1972).
49. Dhakal, S., Reiter, J. W., Laroche, A. & Schultz, E. A. Leaf vein pattern response to heat and drought requires genes that influence pinformed1 localization and is mimicked by aba treatment. *Environ. Exp. Bot.* **185**, 104426 (2021).
50. Mitchison, G. The dynamics of auxin transport. *Proc. R. Soc. Lond. Ser. B. Biol. Sci.* **209**, 489–511 (1980).
51. Mitchison, G. The polar transport of auxin and vein patterns in plants. *Philos. Trans. R. Soc. Lond. B, Biol. Sci.* **295**, 461–471 (1981).
52. Galweiler, L. et al. Regulation of polar auxin transport by atpin1 in Arabidopsis vascular tissue. *Science* **282**, 2226–2230 (1998).
53. Mattsson, J., Sung, Z. R. & Berleth, T. Responses of plant vascular systems to auxin transport inhibition. *Development* **126**, 2979–2991 (1999).
54. Scarpella, E., Marcos, D., Friml, J. & Berleth, T. Control of leaf vascular patterning by polar auxin transport. *Genes Dev.* **20**, 1015–1027 (2006).
55. Marcos, D. & Berleth, T. Dynamic auxin transport patterns preceding vein formation revealed by live-imaging of Arabidopsis leaf primordia. *Front. Plant Sci.* **5**, 235 (2014).
56. Yagi, H., Tamura, K., Matsushita, T. & Shimada, T. Spatiotemporal relationship between auxin dynamics and hydathode development in Arabidopsis leaf teeth. *Plant Signal. Behav.* **16**, 1989216 (2021).
57. Yagi, H. et al. Fluorescent protein-based imaging and tissue-specific RNA-Seq analysis of Arabidopsis hydathodes. *J. Exp. Bot.* **72**, 1260–1270 (2021).
58. Routaboul, J.-M. et al. Arabidopsis hydathodes are sites of intense auxin metabolism and nutrient scavenging. *bioRxiv* (2022).
59. Stoma, S. et al. Flux-based transport enhancement as a plausible unifying mechanism for auxin transport in meristem development. *PLoS Comput. Biol.* **4**, e1000207 (2008).
60. Cieslak, M., Runions, A. & Prusinkiewicz, P. Auxin-driven patterning with unidirectional fluxes. *J. Exp. Bot.* **66**, 5083–5102 (2015).
61. Hartmann, F. P., Barbier de Reuille, P. & Kuhlemeier, C. Toward a 3d model of phyllotaxis based on a biochemically plausible auxin-transport mechanism. *PLoS Comput. Biol.* **15**, e1006896 (2019).
62. Ravichandran, S. J., Linh, N. M. & Scarpella, E. The canalization hypothesis–challenges and alternatives. *N. Phytol.* **227**, 1051–1059 (2020).
63. Merks, R. M. H., Van de Peer, Y., Inzé, D. & Beemster, G. T. S. Canalization without flux sensors: a traveling-wave hypothesis. *Trends Plant Sci.* **12**, 384–390 (2007).
64. Althuis, J. *Auxin waves in a two-dimensional grid*. BSc thesis, Leiden University (2021).
65. Bilsborough, G. D. et al. Model for the regulation of *Arabidopsis thaliana* leaf margin development. *Proc. Natl. Acad. Sci.* **108**, 3424–3429 (2011).
66. Boots, B., Sugihara, K., Chiu, S. N. & Okabe, A. *Spatial tessellations: concepts and applications of Voronoi diagrams* (John Wiley & Sons, 2009).
67. Martinez, C. C., Koenig, D., Chitwood, D. H. & Sinha, N. R. A sister of PIN1 gene in tomato (*Solanum lycopersicum*) defines leaf and flower organ initiation patterns by maintaining epidermal auxin flux. *Dev. Biol.* **419**, 85–98 (2016).
68. Scarpella, E., Barkoulas, M. & Tsiantis, M. Control of leaf and vein development by auxin. *Cold Spring Harb. Perspect. Biol.* **2**, a001511 (2010).
69. Lavania, D., Linh, N. M. & Scarpella, E. Of cells, strands, and networks: auxin and the patterned formation of the vascular system. *Cold Spring Harb. Perspect. Biol.* **13**, a039958 (2021).
70. Vieten, A. et al. Functional redundancy of PIN proteins is accompanied by auxin-dependent cross-regulation of PIN expression. *Development* **132**, 4521–4531 (2005).
71. Bellenot, C., Routaboul, J.-M., Laufs, P. & Noël, L. D. Hydathodes. *Curr. Biol.* **32**, R763–R764 (2022).
72. Routaboul, J. -m et al. Arabidopsis hydathodes are sites of auxin accumulation and nutrient scavenging. *Plant J.* **120**, 857–871 (2024).

73. Sánchez-Vicente, I., Lechón, T., Fernández-Marcos, M., Sanz, L. & Lorenzo, O. Nitric oxide alters the pattern of auxin maxima and pin-formed1 during shoot development. *Front. Plant Sci.* **12**, 630792 (2021).
74. Linh, N. M. & Scarpella, E. Leaf vein patterning is regulated by the aperture of plasmodesmata intercellular channels. *PLoS Biol.* **20**, e3001781 (2022).
75. Band, L. R. Plasmodesmata play a key role in leaf vein patterning. *PLoS Biol.* **20**, e3001806 (2022).
76. Sawchuk, M. G. & Scarpella, E. Control of vein patterning by intracellular auxin transport. *Plant Signal. Behav.* **8**, e1003294 (2013).
77. Verna, C., Sawchuk, M. G., Linh, N. M. & Scarpella, E. Control of vein network topology by auxin transport. *BMC Biol.* **13**, 94 (2015).
78. Heisler, M. G. et al. Patterns of auxin transport and gene expression during primordium development revealed by live imaging of the Arabidopsis inflorescence meristem. *Curr. Biol.* **15**, 1899–1911 (2005).
79. Chen, C.-C. & Chen, Y.-R. Study on laminar hydathodes of Ficus formosana (Moraceae) ii. morphogenesis of hydathodes. *Botanical Stud.* **47**, 279–292 (2006).
80. LERSTEN, N. R. & PETERSON, W. H. Anatomy of hydathodes and pigment disks in leaves of Ficus diversifolia (Moraceae). *Botanical J. Linn. Soc.* **68**, 109–113 (1974).
81. Lersten, N. & Curtis, J. Laminar hydathodes in urticaceae: survey of tribes and anatomical observations on Pilea pumila and Urtica dioica. *Plant Syst. Evol.* **176**, 179–203 (1991).
82. Kneuper, I. et al. Auxin biosynthesis and cellular efflux act together to regulate leaf vein patterning. *J. Exp. Bot.* **72**, 1151–1165 (2021).
83. Runions, A. et al. Modeling and visualization of leaf venation patterns. *ACM Trans. Graph.* **24**, 702–711 (2005).
84. Feugier, F. G. & Iwasa, Y. How canalization can make loops: a new model of reticulated leaf vascular pattern formation. *J. Theor. Biol.* **243**, 235–244 (2006).
85. Ronellenfitsch, H. & Katifori, E. Global optimization, local adaptation, and the role of growth in distribution networks. *Phys. Rev. Lett.* **117**, 138301 (2016).
86. Ronellenfitsch, H. & Katifori, E. Phenotypes of vascular flow networks. *Phys. Rev. Lett.* **123**, 248101 (2019).
87. Owens, A. et al. The hidden diversity of vascular patterns in flower heads. *New Phytol* **243**, 423–439(2024).
88. Zwieniecki, M. A., Melcher, P., Boyce, C. K., Sack, L. & Holbrook, N. Hydraulic architecture of leaf venation in laurus nobilis l. *Plant, Cell Environ.* **25**, 1445–1450 (2002).
89. Cochard, H., NARDINI, A. & Coll, L. Hydraulic architecture of leaf blades: where is the main resistance? *Plant, Cell Environ.* **27**, 1257–1267 (2004).
90. Ronellenfitsch, H. Optimal elasticity of biological networks. *Phys. Rev. Lett.* **126**, 038101 (2021).
91. Turing, A. M. The chemical basis of morphogenesis. *Bull. Math. Biol.* **52**, 153–197 (1990).
92. Sheth, R. et al. Hox genes regulate digit patterning by controlling the wavelength of a turing-type mechanism. *Science* **338**, 1476–1480 (2012).
93. Ding, B. et al. Two MYB proteins in a self-organizing activator-inhibitor system produce spotted pigmentation patterns. *Curr. Biol.* **30**, 802–814 (2020).
94. Wolpert, L. Positional information and the spatial pattern of cellular differentiation. *J. Theor. Biol.* **25**, 1–47 (1969).
95. Wolpert, L. Positional information and pattern formation. *Curr. Top. Dev. Biol.* **6**, 183–224 (1971).
96. Wolpert, L. Positional information and pattern formation. *Curr. Top. Dev. Biol.* **117**, 597–608 (2016).
97. Friml, J. Auxin transport—shaping the plant. *Curr. Opin. plant Biol.* **6**, 7–12 (2003).
98. Berleth, T., Scarpella, E. & Prusinkiewicz, P. Towards the systems biology of auxin-transport-mediated patterning. *Trends Plant Sci.* **12**, 151–159 (2007).
99. Cieslak, M., Owens, A. & Prusinkiewicz, P. Computational models of auxin-driven patterning in shoots. *Cold Spring Harb. Perspect. Biol.* **14**, a040097 (2022).
100. Vasco, A., Thadeo, M., Conover, M. & Daly, D. C. Preparation of samples for leaf architecture studies, a method for mounting cleared leaves. *Appl. Plant Sci.* **2**, 1400038 (2014).
101. Dirnberger, M., Kehl, T. & Neumann, A. Nefi: network extraction from images. *Sci. Rep.* **5**, 1–10 (2015).
102. Capretto, T. et al. Bambi: a simple interface for fitting Bayesian linear models in Python. *J. Stat. Softw.* **103**, 1–29 (2022).
103. Makowski, D., Ben-Shachar, M. S., Chen, S. A. & Lüdecke, D. Indices of effect existence and significance in the Bayesian framework. *Front. Psychol.* **10**, 2767 (2019).
104. Green, P. J. & Sibson, R. Computing Dirichlet tessellations in the plane. *Computer J.* **21**, 168–173 (1978).
105. Bentley, J. L. Multidimensional binary search trees used for associative searching. *Commun. ACM* **18**, 509–517 (1975).
106. Pedmale, U. V. & Liscum, E. Regulation of phototropic signaling in Arabidopsis via phosphorylation state changes in the phototropin 1-interacting protein nph3. *J. Biol. Chem.* **282**, 19992–20001 (2007).
107. Boutté, Y., Crosnier, M.-T., Carraro, N., Traas, J. & Satiat-Jeunemaitre, B. The plasma membrane recycling pathway and cell polarity in plants: studies on pin proteins. *J. Cell Sci.* **119**, 1255–1265 (2006).
108. Pasternak, T. et al. Protocol: an improved and universal procedure for whole-mount immunolocalization in plants. *Plant Methods* **11**, 50 (2015).
109. Schindelin, J. et al. Fiji: an open-source platform for biological-image analysis. *Nat. methods* **9**, 676–682 (2012).
110. Karwowski, R. & Prusinkiewicz, P. Design and implementation of the L+C modeling language. *Electron. Notes Theor. Computer Sci.* **86**, 134–152 (2003).

Acknowledgements

We thank Kyle Schlecht and Tim Mulligan for plant care and maintenance; Tara Skopelitis and Dr. Fay-wei Li for sharing Marchantia tissue samples; Dr. Jan Traas and Dr. Thu Tran for sharing the anti-PIN serum; Dr. Iacopo Gentile for help designing leaf clearing protocols; Dr. Jia He and Dr. Erika Wee for help with microscopy and imaging; Brendan Brozen for help with tracing; and Dr. Taehoo Ha and Dr. Carlos Martí-Gómez for suggestions on statistical testing; and Dr. Mikolaj Cieslak for supporting vlab. We thank the Martienssen Lab and the Lippman Lab for sharing imaging resources and plant materials. XZ extends her appreciation to thesis committee members, especially Dr. David McCandlish for their support and constructive feedback. William R. Miller Fellowship at the School of Biological Sciences at Cold Spring Harbor Laboratory (XZ). NIH grant R35GM125003 (UVP). NSF awards IOS-2224874 and 2131631 (DJ). Natural Sciences and Engineering Research Council of Canada Discovery Grant 2019-06279 (PP). National Science Foundation under award CAREER DBI-1846554 (SN). Funding from the Simons Center for Quantitative Biology at Cold Spring Harbor Laboratory (SN).

Author contributions

Conceptualization: X.Z., E.B., P.P., S.N. Experiments: X.Z., S.P., M.V., U.V.P., D.J., E.S. Statistical tests & data analysis: X.Z., S.N. Computational model: P.P., X.Z. Writing - original draft: X.Z., P.P., S.N. Writing - review & editing: X.Z., S.P., E.B., M.V., U.V.P., D.J., E.S., P.P., S.N.

Competing interests

The authors declare no competing interests.

Additional information

Supplementary information The online version contains supplementary material available at (https://doi.org/10.1038/s41467-026-71768-3).

Correspondence and requests for materials should be addressed to Przemyslaw Prusinkiewicz or Saket Navlakha.

Peer review information *Nature Communications* thanks Takaaki Yonekura, and the other, anonymous, reviewer(s) for their contribution to the peer review of this work. A peer review file is available.